

A Study of the Potential for Gamma Rays to Mimic WIMP Signals in DEAP-3600

by

Catherine Elizabeth Bina

A thesis submitted in partial fulfillment of the requirements for the degree of

Master of Science

Department of Physics

University of Alberta

Abstract

Identification of, and discrimination against, background radiation is of the utmost importance in dark matter searches. DEAP-3600 (Dark Matter Experiment using Argon Pulse shape discrimination) is a single phase, direct dark matter detector with a 3300 kg liquid argon target housed in a spherical acrylic vessel viewed by 255 photomultiplier tubes (PMTs). It is used to search for spin independent interactions of Weakly Interacting Massive Particle (WIMP) dark matter with the liquid argon nuclei. The measured energy resolution represents the detector's ability to distinguish between sources of ionizing radiation. This is determined to be $3.92 \pm 0.09\%$ in data for the 2.6 MeV gamma line from ^{208}Tl after correcting for the relative efficiencies and channel gain of the PMTs. The simulated energy resolution for the same gamma line is found to be $2.59 \pm 0.02\%$ when the PMTs do not produce afterpulsing and $2.86 \pm 0.02\%$ with the creation of afterpulses. The difference between data and simulation is briefly discussed.

Some of the largest sources of backgrounds in direct dark matter detectors stem from the detector components themselves. This is the case for gamma radiation within DEAP-3600, which is produced primarily by uranium and thorium in the glass of the PMTs. An investigation of false WIMP signals produced by high-energy gamma rays stemming from the PMTs has been conducted with the use of Monte Carlo simulations and is presented in this work. The mechanism by which they are most likely to produce WIMP signals is presented. A comparison of the simulated events in the region of interest (ROI) with events from data is performed. The effect of afterpulsing on an event's probability to be in the ROI

is also studied.

Preface

The work presented in this thesis is original and is the author's own, except where denoted by citations or mentioned below. Specifically, the study of the energy resolution of the DEAP-3600 detector discussed in Chapter 3, the investigation into high-energy gamma rays creating false WIMP signals in Chapter 4 and the conclusions drawn from these analyses are the author's original work.

The design and commissioning of the DEAP-3600 detector, as well as the ongoing data collection, is the result of collaborative effort by the entire DEAP Collaboration. The processors discussed in the body of this thesis are the work of members of the DEAP collaboration. In particular, the *multisite* and *smartcal* processors were developed by Thomas McElroy and implemented in the RAT framework by him with the help of other DEAP collaborators. The code to create the PMT maps shown in Chapter 4 was based on a simpler version written by James Bueno.

*To my parents,
David and Alexa Bina,
for their unconditional love and support,
and for always being my biggest cheerleaders.*

Acknowledgments

This thesis and the work presented within are the culmination of years of hard work, perseverance and the support of family, friends and colleagues. My family and the community that I have become a part of here in Edmonton kept my spirits up when they faltered and provided me with an invaluable support system.

I would like to thank my supervisors, Aksel Hallin and Darren Grant, for taking me on as a graduate student and providing insight and support during my master's program. Your guidance on my research and on teaching has helped shape me into the physicist that I am today. Many thanks to all of my fellow members of the DEAP collaboration for making the experiment what it is and contributing to my graduate experience. I am particularly grateful to Robert Stainforth, James Bueno and my University of Alberta collaborators for their time and assistance.

A special thanks to Yasir Syed for his advice, guidance and investment in my success. The strategies you taught me are invaluable and I am sure that I will be using them for years to come.

I am exceedingly thankful for my fellow graduate students that became close friends along this journey: Sebastian Sanchez, Kirsty Gardner, Annika Rosanowski, Sourav Sarkar, Michelle Sullivan, Titash Choudhury and Charles Jensen. You have seen me at my best and my most stressed and I'm grateful to have had your friendship through it all. I am especially thankful for Sebastian, who believes in me and my abilities unwaveringly and helps me to have that same faith in myself. You are like a brother to me and I cannot imagine you

not being a part of my life. A special thank you to Kirsty and Annika as well, for your great friendship and support (and for sharing your pets with me). I have enjoyed co-hosting Canadian Thanksgiving with you.

For making Edmonton truly feel like a home and keeping me sane, I would like to thank all of my friends at KPC Self Defense. A special thank you to Randy King, Michelle Hanlon and Thor for making KPC more than just a gym, but a community, and providing me with a sense of belonging up here. To Heidi Heinz, thank you for being my best friend, my confidant, my partner in crime and for making sure I don't take myself too seriously. Thank you to Sam Leier for giving me advice and encouragement, especially during the writing process, and for making sure I remember to go out and have fun with friends. And thank you to Cara McInnis for your support and placating my irrational side when I was stressed.

Lastly, none of this would have been possible without the love and support of my family. I have unending gratitude for my parents. You taught me to always try my best and provided me with the unconditional love and encouragement that I needed to accomplish that. I would also like to thank my grandparents, especially Papa and Grandpa Don, my Aunt Denise and my Aunt Janet for their support and for always taking an interest in my life and what I am doing.

Thank you again to everyone who has been there for me on this journey. It has meant more than I can say to know that I have so many people in my corner.

Contents

Abstract	ii
Preface	iv
Acknowledgments	vi
1 Introduction	1
1.1 Dark Matter in Particle Physics	2
1.2 Direct Detection of Dark Matter	3
2 Scintillation of Noble Liquids and The DEAP Experiment	6
2.1 The Scintillation Process	6
2.2 Description of DEAP-3600 Detector	9
2.2.1 Inner Detector	11
2.2.2 Data Acquisition System	12
2.2.3 Outer Detector	13
2.2.4 Neck	13
2.3 Background Contamination	15
2.3.1 Alpha Particles	15
2.3.2 Neutrons	18
2.3.3 Beta Decays and Gamma Rays	18
3 Energy Resolution	20
3.1 Measured Gamma Ray Energy Resolution	20
3.2 Simulating Gamma Rays in the DEAP-3600 Detector	28
4 Investigating Gamma Ray Leakage Events in DEAP-3600	32
4.1 Leakage Events	32
4.2 Modifications to the Simulation	33
4.3 Leakage Event Behavior	34
4.4 Comparing the DEAP-3600 Detector Simulation to Data	43
4.5 Effect of Afterpulsing on Leakage Events	48
5 Conclusion	51
References	53

A Sample Track

58

List of Tables

2.1	Properties of Liquid Argon and Liquid Xenon	9
3.1	Cuts Performed to Create Gamma Skim Files	21
3.2	Fit Results for Run 18024	27
3.3	Energy Resolutions for Run 18024	28
3.4	Energy Resolutions for Full Detector Simulations	30
4.1	Leakage Event Track Summary	35
4.2	Cuts Performed to Create Survivor Events Dataset	44
4.3	Leakage Events that Survive Cuts	47
4.4	Percentage of Total Events Removed By Cuts	48
4.5	Percentage of Scintillation Leakage Events Removed by Cuts	50

List of Figures

1.1	Limits on the Spin Independent WIMP-nucleon Cross Section	4
2.1	F_{prompt} versus Energy Distinguishing the Nuclear and Electronic Recoil Bands	8
2.2	Diagram of DEAP-3600	10
2.3	Diagram of the Neck of the Detector	14
2.4	Primordial ^{232}Th Decay Chain	16
2.5	Primordial ^{238}U Decay Chain	17
3.1	Single Photoelectron Pulse in ADC	22
3.2	Raw Charge Spectrum of Gamma Rays	22
3.3	Gain Corrected Charge Spectrum of Gamma Rays	23
3.4	Relative Efficiency Corrected Raw Charge Spectrum of Gamma Rays	25
3.5	Relative Efficiency and Gain Corrected Charge Spectrum of Gamma Rays	25
3.6	Event qPE Spectrum of Gamma Rays	26
3.7	Sample Components and Initial Parameters of Energy Resolution Fit	27
3.8	Event qPE Spectra for Simulated ^{208}Tl Peak With and Without AP	30
3.9	Full Detector Gamma Simulation F_{prompt} vs Event qPE - Energy from 60-21500 PE	31
3.10	Full Detector Gamma Simulation F_{prompt} vs Event qPE - Energy from 0-240 PE	31
4.1	Partial Fill Gamma Simulation Without AP F_{prompt} vs Event qPE with Regions Labeled	33
4.2	Partial Fill Gamma Simulation F_{prompt} vs Event qPE - Leakage Events	35
4.3	Z vs ρ of Partial Fill Leakage Event Interactions	36
4.4	Distribution of FmaxPE for Leakage Events With LAr Scintillation Versus No LAr Scintillation	37
4.5	PMT Maps for Pure Cherenkov Events	39
4.6	PMT Map for Mixed Cherenkov and Scintillation Light	40
4.7	PMT Maps of Total, Prompt and Late Light for Mixed Cherenkov and Scintillation Interactions	42
4.8	Leakage Events Overlaid on Survivor Events	43
4.9	Distribution of FmaxPE Late for Leakage Events and Survivor Events	45
4.10	Distribution of FmaxPE NN for Leakage Events and Survivor Events	46
4.11	Comparison of Data and MC with Thorium Source	47

4.12 Partial Fill Gamma Simulation F_{prompt} vs Event qPE - Energy From 60-21500 PE	49
4.13 Partial Fill Gamma Simulation F_{prompt} vs Event qPE - Energy from 0-500 PE	50

Chapter 1

Introduction

The observation of gravitational effects on astronomical objects has both led to discoveries and been used to confirm theories. In 1844, Friedrich Wilhelm Bessel announced that the stars Sirius and Procyon were members of binary systems with invisible companions of mass similar to their own [1]. Based on observed periodic position shifts relative to other stars, he correctly estimated their orbital periods to be approximately 50 years [2]. Visible confirmation of the existence of one of the companions, Sirius B, was observed by Alvan G. Clark in 1862 [1]. Observed gravitational effects were also used to confirm Einstein's theory of general relativity that predicted the deflection of light caused by the curving of space around the Sun. This was later confirmed during a solar eclipse in 1919 in what is now considered the first observation of gravitational lensing [3]. Less than 20 years later, gravitational effects from unseen matter would be observed by both Fritz Zwicky and Jan Oort. Oort found that the number of visible stars near the Sun were 30-50% lower than necessary to account for their velocities in 1932 [1]. In 1933, Zwicky observed that the velocity dispersion of galaxies in the Coma cluster would require the cluster to have an average density 400 times the density of the luminous matter [4]. Both used the term "dark matter" to describe this missing mass.

While the term dark matter can be traced back to the early 1930s, its existence was not widely accepted by the professional astronomical community until 1978, when Vera Rubin and Kent Ford showed that the rotation of the outer regions of the galaxy M31 required significant amounts of invisible mass to rotate at a similar velocity as the central regions [5]. Over the course of the next decade, research continued to indicate the existence of dark matter halos surrounding each galaxy and began to support the idea that it was made up of some undiscovered subatomic particle, fostering some of the first collaborations between astrophysicists and particle physicists [6]. Research in the 1990s and 2000s have continued to provide support for the existence of dark matter over alternatives such as

different gravitational theories. Some of this research has included observations of both strong and weak gravitational lensing, the Cosmic Microwave Background, hot gas in galaxy clusters, distant supernovae and collisions of galaxy clusters [7]. Data from these experiments have also provided many of the constraints on dark matter and its possible candidates under consideration today.

In 1990, Canadian astronomer Sidney van den Bergh declared that "Cosmology is in chaos" and placed part of the blame on the nature of dark matter being a "complete mystery" that constituted 90 to 99% of the matter of the universe [8]. Based on the 2015 Planck results, dark matter accounts for 25.8% of the energy density of the universe, with only 4.8% comprised of baryonic (or ordinary) matter, meaning that dark matter is responsible for $\approx 84.3\%$ of the matter in the universe [9]. But beyond that, the nature of dark matter remains elusive, with astronomers and particle physicists around the world still working to understand it.

1.1 Dark Matter in Particle Physics

A leading candidate for dark matter is the Weakly Interacting Massive Particle (WIMP) [10]. WIMPs are favored due to their prevalence in particle physics theories, their ability to be detected in multiple ways and the fact that they have a predicted naturally occurring relic density consistent with the observed energy density of dark matter [7]. (This thesis will focus on the search for WIMPs and any references to dark matter can be taken as synonymous to WIMPs.) WIMPs are stable particles that only interact weakly and have a mass in the 10 GeV-TeV range [7]. However, when using the assumption that the Milky Way's dark matter halo is composed solely of WIMPs, the mass range is limited to the 100 GeV-1 TeV range [7]. This, combined with the canonical local WIMP density of 0.3 GeVcm^{-3} , sets the WIMP flux at the Earth to $\approx 10^4\text{-}10^5 \text{ WIMPs cm}^{-2}\text{s}^{-1}$ [11].

WIMPs can be studied via production in particle colliders, indirect detection and direct detection. Particle colliders such as the LHC have the possibility of producing WIMPs from the collision of two standard model (SM) particles. If the collision produced both WIMPs and SM particles, then the SM particle would be detected while the missing transverse energy and momentum would provide the dark matter signature [7]. Both ATLAS and CMS are searching for dark matter signatures from both specific theories, such as supersymmetry, and model-independent scenarios [12].

Indirect detection experiments search for SM products from the annihilation or decay of WIMPs. Some of the SM products being searched for are neutrinos, antimatter and gamma rays. Neutrino detectors, such as IceCube Neutrino Observatory [13] and Super-Kamiokande

detector [14], look for an excess of neutrinos coming from the Sun or the center of the galaxy. This excess could be due to WIMPs that scattered off nuclei while passing through the Sun or galactic center. Subsequent scatters would slow the WIMP enough to get captured in its gravitational pull and eventually decay or annihilate, producing a SM particle excess [7]. Gamma ray and antimatter experiments search for dark matter annihilation products with galactic origins [7].

Direct dark matter detection searches for evidence of WIMPs elastically scattering from nuclei. Energy is deposited during this interaction, causing nuclear recoils (NR). These detectors aim to distinguish between recoil energy coming from WIMP interactions and recoils caused by background radiation. Recoil energy may be detected as light, charge or heat, depending on the target material, with some experiments able to measure two of these forms of energy [15].

1.2 Direct Detection of Dark Matter

The WIMP flux at the Earth is expected to be large enough that a small amount of WIMPs may elastically scatter off nuclei in large, dense target materials. The interaction rate is expected to be less than 1 event per 10 kg of target material per day [16], however, leading to detectors being located deep underground in order to minimize the backgrounds from cosmic ray activity, that would overwhelm WIMP signals in detectors on the surface. Even when located deep underground, low absolute background levels and effective discrimination strategies are required [17]. Shielding of the target mass and high radiopurity of all detector materials are used to ensure low backgrounds. Discrimination strategies often employ the rejection of backgrounds based on the expected behavior of WIMPs and backgrounds in the detector. These methods include rejection of events that occur near the surface of the detector, as backgrounds are more likely to interact in those regions while WIMPs interact uniformly in the volume, and rejection of events with multiple interactions since WIMPs do not interact strongly enough to scatter more than once in a detector [16]. Another strategy is based on WIMPs having a high tendency to only interact with an atom's nuclei [16]. Using this fact, experiments can reject interactions with atomic electrons (electronic recoils—ER). How this discrimination is performed depends on the signal created by recoils in the detector.

Direct dark matter detectors can be categorized either by the signal(s) they detect or by the detector type—determined by a combination of the target material and the method of detection. There are five main detector categories: threshold, scintillating crystals, liquid noble gas, cryogenic and directional. Current results for some direct dark matter detectors are shown in Figure 1.1. Following are brief explanations of the detector types, along with

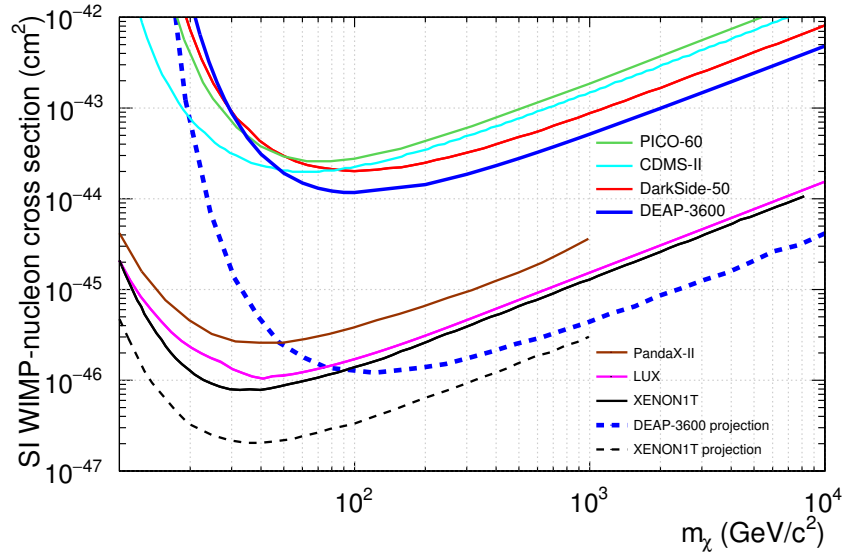


Figure 1.1: Current limits on the spin independent WIMP-nucleon cross section [10]. The DEAP results are from 4.44 live days of data with a 90% confidence level exclusion.

some examples.

Threshold detectors use superheated liquids in either bubble chambers or droplet detectors [18]. Recoil energy is deposited as heat in the target. Sufficient amounts of energy cause bubble nucleation, which is photographed [18]. Electronic recoils are not a background in these detectors as they do not provide a dense enough energy deposition to induce nucleation [16]. Strategies are needed to distinguish between NR from WIMPs and NR from alphas and neutrons. PICO-60 is a threshold detector using superheated C_3F_8 in a bubble chamber at SNOLAB. The experiment uses acoustic signals in combination with camera images from an event to discriminate against alpha decays and the creation of multiple bubbles to discriminate against neutron interactions [19].

Scintillating crystal detectors use inorganic crystals to detect light caused by recoil energy. Background rejection can only be performed by rejecting multiple scatter events in some experiments [18], while others, like the KIMS Experiment, also employ pulse shape discrimination (PSD) [20]. They look for an annual modulation in the event rate of very low energy single scatters, which is predicted for halo WIMPs due to the Earth moving around the Sun [16]. The DAMA/LIBRA experiment has claimed detection of WIMPs, but this result has yet to be confirmed by other experiments and is in conflict with some limits set by other detectors [16].

Liquid noble gas detectors search for nuclear recoils from WIMPs using either scintillation or scintillation and ionization. These two methods are categorized as single phase—in which

the target medium is solely liquid—and dual phase—where both the liquid and gaseous states are used in the target medium. Interactions in the detector cause excitation and ionization of the target material. Both experiment types detect the primary scintillation signal created in the liquid. The timing information of the light pulse combined with the light detected can be used in PSD, which is the primary background rejection method employed by single phase detectors, *e.g.* DEAP-3600 (see Section 2.1). As a single phase detector, this is the strategy used by DEAP-3600 and will be expanded upon in Section 2.1. Dual phase experiments, such as DarkSide-50 and XENON1T, are time projection chambers that drift the electrons from ionization upward into the gaseous region via an electric field. The electrons then enter the gaseous region and are detected as proportional light [21]. The ratio of the secondary to primary signal is different for NR and ER and is therefore also utilized for background discrimination.

Cryogenic detectors are solid state detectors whose primary signal is either phonons or charge. Some are solely ionization detectors, such as CoGeNT [16]. These are cooled to the temperature of liquid nitrogen, 77 K, and search for annual modulation of the measured event rate [18]. More commonly, cryogenic detectors measure recoil energy as phonons, either by collecting the non-thermal phonons or measuring the temperature change caused by the thermal phonons [16]. This class of cryogenic detector is typically operated at temperatures below 1 K. There are two component detectors that also collect either charge signals, as in CDMS and EDELWEISS, or scintillation signals, as in CRESST [18][20].

The last category discussed here are directional detectors. These detectors measure the direction and ionization density of recoil tracks in gaseous time projection chambers [18]. Experiments such as DRIFT-II expect to see an asymmetry in the number of events scattering forwards and backwards, due to the Earth moving through the Milky Way dark matter halo, leading to a directional bias of WIMPs seeming to originate from the Cygnus constellation [18].

This is just a snapshot of the direct dark matter detectors and their techniques. This thesis will center on research performed for the DEAP-3600 experiment. Chapter 2 will begin with an explanation of the scintillation process in liquid noble gases and the background discrimination strategy in single phase detectors. Following that, it will describe the DEAP detector and associated backgrounds. Chapter 3 focuses on the measured DEAP-3600 energy resolution from the gamma spectrum, in data and simulation, with an emphasis on gammas originating in the photomultiplier tubes (PMTs). The potential for those gammas to create WIMP-like signals is explored in Chapter 4, concluding with strategies for future research in the topic.

Chapter 2

Scintillation of Noble Liquids and The DEAP Experiment

This chapter begins with an explanation of the scintillation mechanism and the choice to use argon in a direct detection search. It will then give a description of the DEAP-3600 detector and its principle of detection. The last section of this chapter is devoted to discussion of the backgrounds in the detector and how they are mitigated.

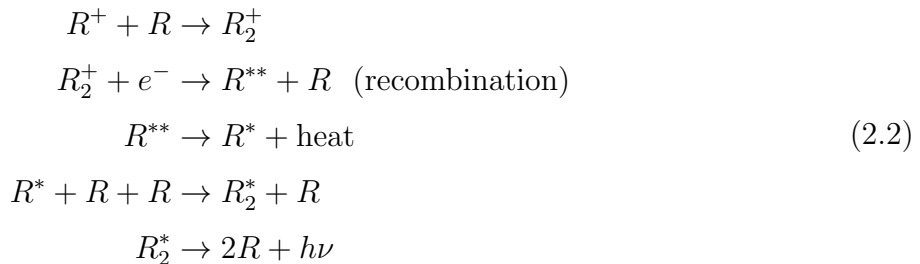
2.1 The Scintillation Process

Liquid noble gases have multiple properties that make them favorable for dark matter detection. They can be relatively easily extracted from the atmosphere and purified, leading to the ability to create large, homogeneous targets [22]. At present, liquid argon (LAr) and liquid xenon (LXe) are the primary choices of dark matter experiments. Liquid neon has been used in the past, but is not discussed here as it is not used in any operating or proposed experiments [23]. As discussed in Section 1.2, recoil energy can be deposited in the detector from particles scattering off the nuclei (NR) or the atomic electrons (ER), and discrimination between NR and ER is essential. This energy deposition can cause excitation or ionization of liquid noble gas atoms. The scintillation processes for these two situations are shown in Equation (2.1) and Equation (2.2), respectively, with R representative of any noble gas, and $h\nu$ denoting the scintillation photon [24].



In Equation (2.1), ionizing radiation excites an atom forming an exciton, R^* . The exciton

forms a strongly bound diatomic molecule with a ground state atom, called an excimer or excited dimer, R_2^* [25].



In Equation (2.2), ionizing radiation ionizes an atom, R^+ , that bonds with a ground state atom to form a diatomic ion, R_2^+ , seen in the first line of Equation (2.2). Recombination with an electron released by the ionization of a neighboring atom causes the diatomic ion to form a highly excited atom, R^{**} [22]. This atom de-excites to the lowest exciton state non-radiatively. The exciton can then form an excimer in the same fashion as Equation (2.1). Scintillation photons are emitted when the excimer de-excites, shown in the last line of Equations (2.1) and (2.2). This de-excitation also disbands the molecule since liquid noble gas atoms are repulsive in the ground state.

The excimers formed can be in one of the two lowest excited states; the singlet or triplet state. The state of the excimer is important for the timing of the light pulse. Singlet states can directly transition to the ground state, giving them a short lifetime. The de-excitation of the triplet state is a forbidden transition due to the triplet excimer having a total spin of 1 while the ground state atoms have a total spin of 0 [26], requiring a spin flip in order to decay, extending its lifetime [27]. The ratio of singlet to triplet state excimers created due to a particle interaction depends on the linear energy transfer (LET) of the particle (i.e. the amount of energy transferred to the target material per unit of distance). More singlet than triplet states are populated as the LET increases [28]. Nuclei recoil with a much slower velocity than electrons, causing them to deposit their energy more densely and so with a higher LET [16]. This means that excimers created from NR are predominately in the singlet state while ER produce mainly triplet state excimers. Due to this distribution and the lifetimes of the two states, NR have a faster pulse shape than ER.

As mentioned in Section 1.2, PSD is a method of background rejection for single phase detectors. With timing as the primary discriminating factor between the scintillation from NR and ER, the discrimination ability is improved with a larger time difference between the singlet and triplet lifetimes. This can be seen in Table 2.1 to be much larger for argon than for xenon. This difference in LAr is large enough that the prompt light signal can be used to determine the relative population of the singlet state, providing identification of the recoil

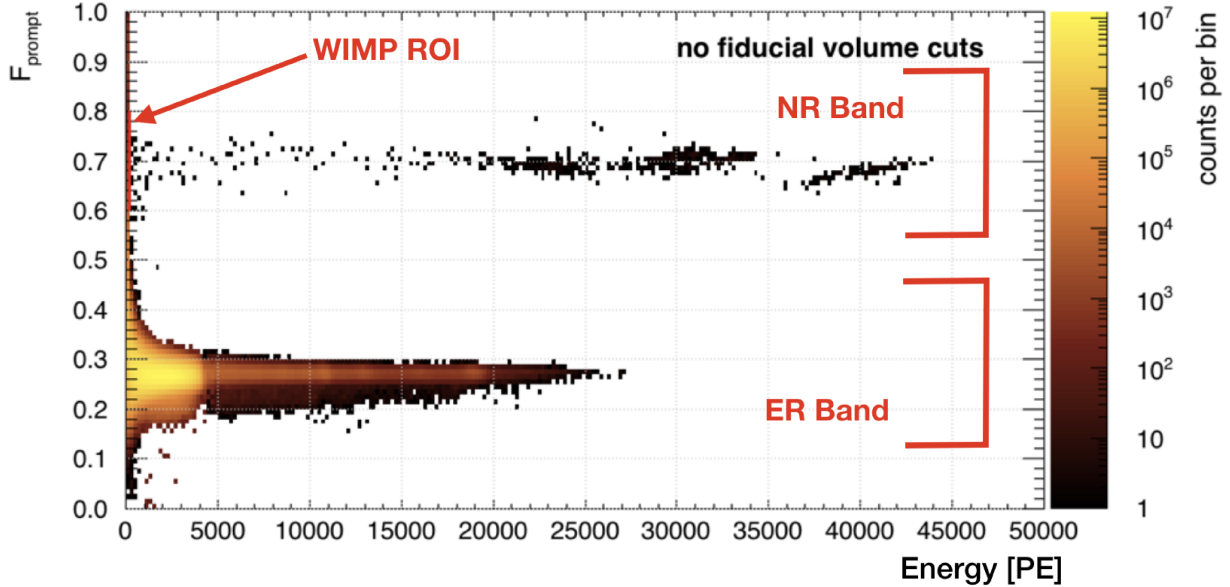


Figure 2.1: F_{prompt} versus energy for 4.7 days of data taking [30], with the nuclear recoil (NR) and electronic recoil (ER) bands highlighted along with the WIMP ROI.

interaction on an event by event basis [29]. The PSD parameter used in DEAP-3600 is called F_{prompt} . It is the fraction of prompt light over total light for the event and is defined as:

$$F_{\text{prompt}} = \frac{\int_{-28ns}^{150ns} Q(t)dt}{\int_{-28ns}^{10000ns} Q(t)dt} \quad (2.3)$$

where $Q(t)$ is the amount of detected light in a given time window measured as the PMT charge in photoelectrons (PE). The times were chosen conservatively in order to make F_{prompt} insensitive to precise time windows. The time window for the total light was chosen to encompass the full light pulse while the prompt timing was selected to be after the singlet light reached the PMTs. As more data is collected, the time windows may be altered to better maximize the separation between nuclear and electronic recoils.

F_{prompt} is often plotted against energy, as shown in Figure 2.1, and two distinct bands can be identified. Nuclear recoils have an F_{prompt} value around 0.7 and form what is known as the NR band, while electronic recoils tend to have $F_{\text{prompt}} \approx 0.3$, forming the ER band. As a PSD parameter, F_{prompt} has demonstrated the ability to suppress ER by a factor of 10^{-10} in the WIMP region of interest (ROI) [30].

In addition to its strength in PSD, LAr has other favorable qualities, some of which are shown in Table 2.1. Its abundance in the atmosphere makes it much more affordable and therefore easier to obtain large volumes. Both argon and xenon have high light yields. Argon,

Table 2.1: Showing some of the properties of Ar and Xe in their liquid phase that are relevant to their use in direct dark matter detectors.

Material	Atomic Number	Singlet Lifetime [ns] [18]	Triplet Lifetime [ns] [18]	Abundance in Atmosphere [ppm] [24]	Light Yield [photons/keV] [21]
Argon	18	6	1600	9340	40
Xenon	54	4	22	0.09	46

with a lower atomic number, is not as good at self shielding as xenon, but that characteristic is not enough to offset the power of its timing based PSD, which ultimately makes it the best choice of target material for single phase detectors.

2.2 Description of DEAP-3600 Detector

DEAP-3600 is a direct detection, dark matter experiment being conducted 2 km underground at SNOLAB in Sudbury, ON, Canada. It is a single phase, liquid argon scintillation detector designed to search for spin independent WIMP dark matter. Its projected sensitivity to the spin independent WIMP-nucleon cross section is 10^{-46} cm² for a WIMP mass of 100 GeV/ c^2 [31]. Due to argon having an even number of protons and neutrons, DEAP-3600 is insensitive to spin dependent interactions [16].

The DEAP-3600 detector can be split into three major components: the inner detector, the outer detector and the neck (see Figure 2.2). The purpose of the inner detector is signal detection and it comprises everything inside of the steel shell: the LAr, wavelength shifter, acrylic vessel (AV), light guides (LGs), filler blocks and PMTs. Scintillation light is wavelength shifted before traveling through the acrylic vessel and light guides to be incident upon one of the 255 PMTs. Once detected, the signal is recorded, digitized and saved to a disk. The outer detector consists of the steel shell, muon veto PMTs, magnetic compensation coils and an 8 m diameter water tank designed for background shielding. The neck serves as both structural and operational integrity, responsible for holding the detector, circulating and cooling the argon, and as the access point to the inner detector. Each of these elements are discussed in detail in the following sections.

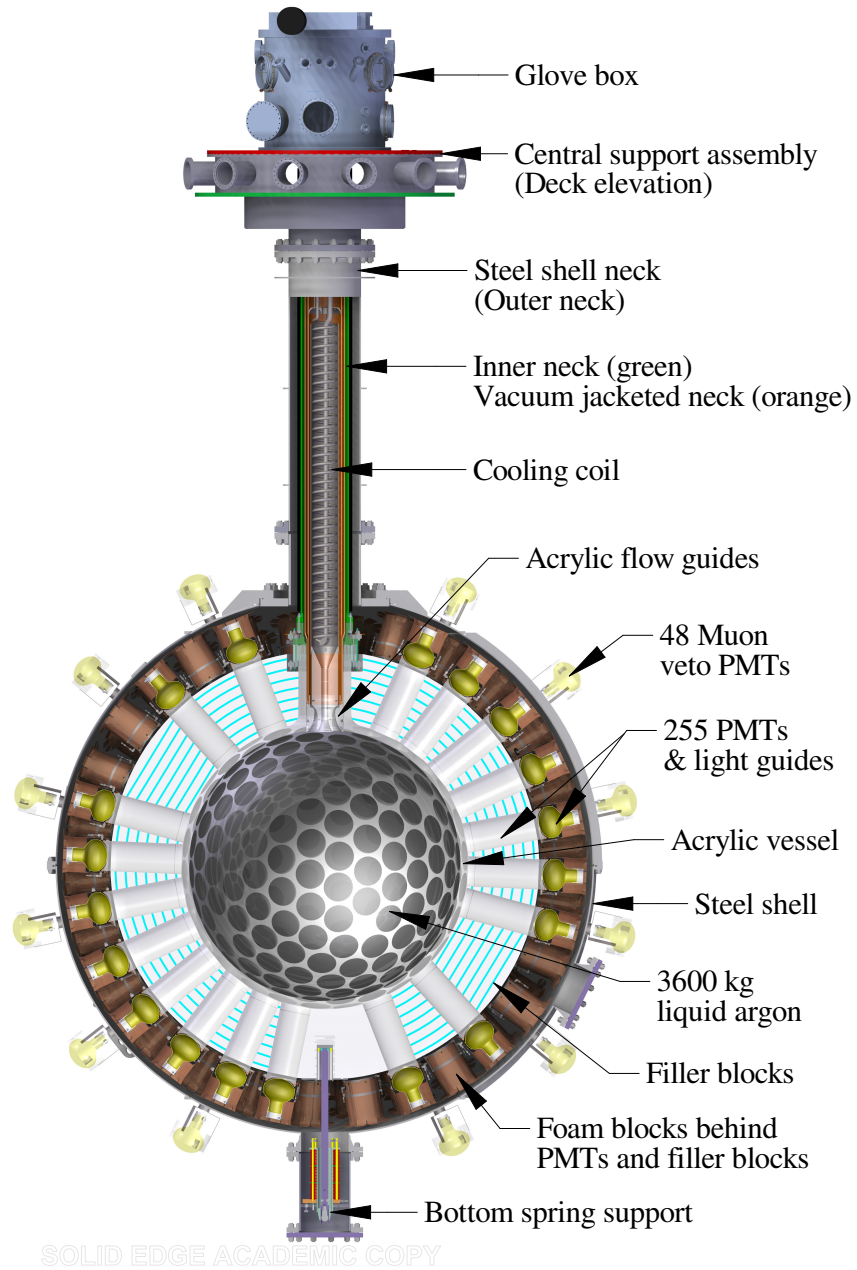


Figure 2.2: A schematic diagram of DEAP-3600 [31] showing the inner detector (acrylic vessel, light guides, filler blocks and PMTs), steel shell, muon veto PMTs and neck. Not shown are the four magnetic compensation coils surrounding this structure and the 8 m diameter water tank that it is suspended in.

2.2.1 Inner Detector

Liquid Argon

DEAP-3600 was originally designed to house 3600 kg of LAr. This was modified due to a neck seal failure, leading to the experiment utilizing 3300 kg of LAr as its target medium. The argon is chemically purified to sub-ppb levels of electronegative impurities by a hot metal getter and then enters a charcoal trap to remove radon and other radioactive impurities to a level low enough that the total volume of LAr has a radon activity of around $5 \mu\text{Bq}$ before it enters the detector volume [31]. The LAr is housed within the AV at a temperature of $\approx 87 \text{ K}$. When a particle interacts within the LAr, scintillation light is emitted in the vacuum ultraviolet range with a peak wavelength at 128 nm [27]. As the corresponding energy is lower than the energy required to excite neutral argon atoms, the scintillation light travels through the LAr without interacting [29].

Acrylic Vessel

The AV that houses the LAr is 85 cm in diameter and 5 cm thick. Acrylic was chosen because it can be produced with high radiopurity, can act as a neutron shield due to its hydrogenous nature, and can handle high thermal gradients [31]. The first two factors are important in dark matter searches due to the need for minimizing radioactivity, expanded upon in Section 2.3. The importance of the latter will become apparent in the discussion of the LGs. The inner surface of the AV is coated with a $3 \mu\text{m}$ layer of 1,1,4,4-tetraphenyl-1,3-butadiene (TPB), an organic wavelength shifter [31]. When the scintillation light reaches the surface of the AV, it is absorbed by the TPB and then re-emitted as visible light. This is necessary due to both the PMTs and the acrylic. The acrylic is opaque to ultraviolet light and the PMTs are made with borosilicate glass that does not transmit radiation below 300 nm [32]. TPB was chosen as it shifts 128 nm light to the visible spectrum with a peak at 420 nm [27], coincident with the peak response wavelength for the PMTs [33] [32].

Light Guides

The AV is surrounded by 255 acrylic LGs bonded to its outer surface. With length of 45 cm and a diameter of 19 cm , they cover $\approx 76\%$ of the surface area of the AV [34]. The remaining AV surface is covered with reflector material that is also wrapped around the LGs in order to retain as much light as possible. Filler blocks occupy the space between the LGs, extending the same length. The filler blocks are composed of alternating layers of high-density polyethylene and Styrofoam brand insulation and serve as both neutron shielding and thermal insulation [31].

The LGs act as a neutron shield for the LAr and as a thermal gradient from the acrylic cryostat to the PMTs, which perform optimally at near room temperature [31]. They also serve to distribute light over the entire PMT surface, which helps average any non-uniformities of the photocathode [35]. Visible light travels through the LGs via total internal reflection until it is incident upon the PMTs.

Photomultiplier Tubes

Each LG has a Hamamatsu R5912 high quantum efficiency PMT optically coupled with silicon oil to the end [34]. These PMTs were chosen for their fast timing response, high detection efficiency and low dark noise rates [31]. The purpose of the PMTs is to detect the scintillation light and convert it into a detectable electrical signal [36]. The PMTs are numbered starting at 0 at the top of the AV and increasing to 254 in a vertical downward spiral. They are operated at temperatures between -35°C and $+5^{\circ}\text{C}$, with the PMTs at the bottom colder than those at the top due to the convection current in the steel shell. Bias voltages between 1400 V and 1800 V are applied to each PMT so that they all have the same gain [34]. Each PMT is magnetically and thermally shielded with a Finemet foil collar and copper collar, respectively. They also receive magnetic shielding from four field-compensating coils located in the water tank [34]. Additionally, polyurethane foam insulation surrounds the PMTs within and around the copper collars for added thermal insulation. All of this is wrapped in a stainless steel mesh, which provides a fail safe to contain pieces of the detector in the event of structural failure [31].

Light incident on a PMT enters the tube through the borosilicate glass that covers the photocathode. The photons strike the photocathode and are converted to electrons (often referred to as photoelectrons—PE) via the photoelectric effect [36]. Ideally, every photon hitting the photocathode would be converted to a single PE. An electric field is applied across the tube to accelerate these PEs to strike a series of dynodes that act as electron multipliers. Secondary electron emission at each dynode multiplies the number of electrons by a factor of five to ten [36]. The number of electrons that are produced by the dynode chain due to a single photon hitting the PMT is known as the PMT’s gain. DEAP-3600’s PMTs have 10 dynodes that provide an average gain of 1×10^7 [34]. The PMT signal is then read out by the data acquisition system (DAQ).

2.2.2 Data Acquisition System

The PMTs are connected to signal conditioning boards (SCBs) via a single cable that both provides the bias voltage and reads out the signal [34]. The SCBs decouple the PMT signal

from the bias voltage and then shape and amplify it into an analog waveform [31]. The analog waveforms are analyzed by the digitizer and trigger module (DTM), which makes the decision to trigger the event readout using a custom field-programmable gate array, with a trigger rate of 3200 Hz [31]. The SCBs also send the analog waveforms to commercial digitizers that digitize the information. If an event is to be read out, the DTM sends a trigger signal to the digitizers that save a 16 μ s digital waveform [37]. The read out rate of the digitizers is 500 Hz [31]. This is much lower than the trigger rate because the main trigger algorithm, the "physics trigger," is set to not read out most of the events caused by ^{39}Ar beta decays [31]. Several front end computers then read and filter the data from the digitizers and the DTM. They bundle the information into a single event that is then saved to disk as a ROOT file [31]. From there the data is immediately sent to an analysis computing cluster for an initial processing to create data quality plots and apply preliminary calibrations and corrections; turning the data into physics units [31]. As calibration and analysis processors are improved, the raw data is reprocessed to create new ROOT files of the corrected data. These are the data files used for physics analyses.

2.2.3 Outer Detector

Contrary to the inner detector, whose primary function is signal detection, the purpose of the outer detector is to shield the inner detector from background contamination and interference. The steel shell acts as a light tight and watertight enclosure for the inner detector [31]. This helps isolate the inner detector from stray photons and protects it when submerged in the water tank. Radon-scrubbed nitrogen gas is continuously purged through the space between the steel mesh surrounding the PMTs and the steel shell [31]. There are 48 PMTs mounted on the outside of the steel shell, as shown in Figure 2.2, and it is suspended within an 8 m diameter ultra-pure water tank. This makes up the muon veto system to detect cosmic ray muons, which produce Cherenkov light as they travel through the water. The water tank also acts as a radiation shield to moderate neutrons coming from the surrounding rock [31]. Within the water tank are four evenly spaced magnetic compensation coils to counteract the ambient magnetic field, preventing it from affecting the collection efficiency of the PMTs [31].

2.2.4 Neck

The steel shell with the inner detector is suspended within the water tank by the outer and inner stainless steel necks, respectively. The outer neck connects the steel shell to the deck above the detector via a central support assembly that allows the detector to move

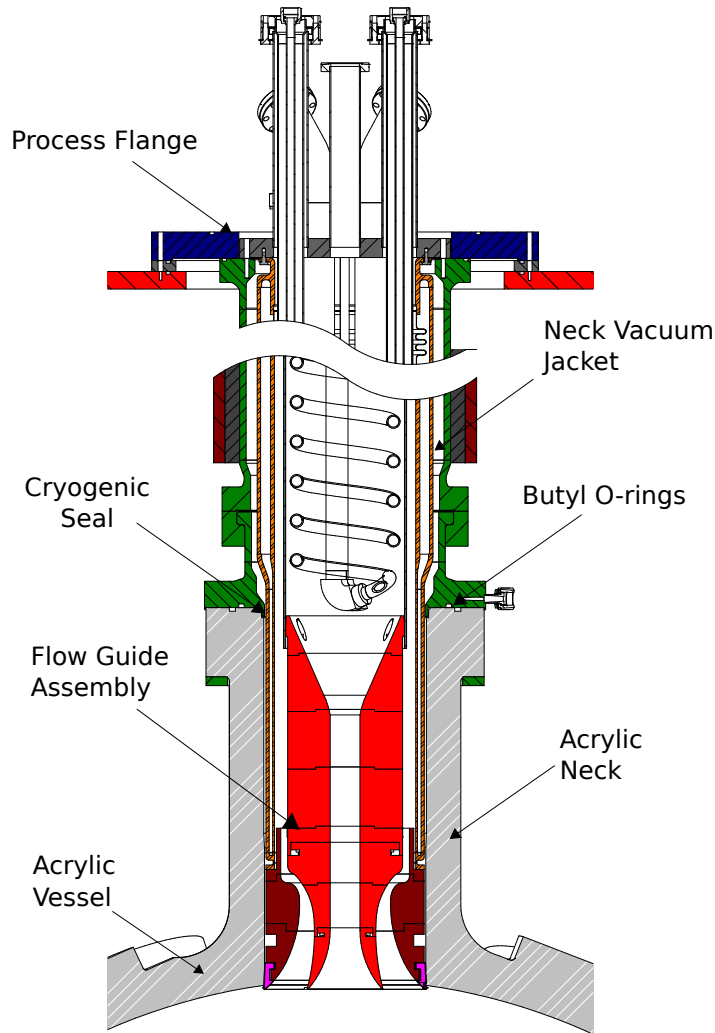


Figure 2.3: Schematic diagram showing the neck of the detector, which contains gaseous argon [31].

slightly during seismic events [31]. Shown in green in Figures 2.2 and 2.3, the steel inner neck supports the inner detector by connecting the AV to the central support assembly. The steel to acrylic connection necessary for this is achieved using butyl o-rings and a cryogenic seal as demonstrated in Figure 2.3 [31].

In addition to providing structural support, the neck serves many operational purposes. The detector is filled with argon via the process flange (blue in Figure 2.3); this is also the means to recirculate the argon through the purification process. A stainless steel cooling coil is suspended in the neck with liquid nitrogen (LN_2) flowing through it to maintain the LAr at a pressure of 13-15 psia and temperature of 84-87 K [31]. The neck is also the access point to the inner detector.

Gaseous argon (GAr) is maintained inside of the neck and in the upper volume of the AV.

Light generated within the GAr or acrylic neck is dealt with in a couple of ways. Some of the light generated in the neck region is blocked by the flow guides located at the bottom of the neck [31]. There are also bundles of optical fibers wrapped around the acrylic neck attached to four PMTs that are used to veto light emitted in the neck region [10]. The final mitigation method is via a fiducial cut performed during the analysis that is based on the fraction of light in the event that is seen in the top two rings of the PMTs (called top2ringsfrac) [30].

2.3 Background Contamination

In scintillation detectors, ionizing radiation causes a signal. This means that for rare, low energy event searches, such as WIMP dark matter searches, background levels must be both very low and effectively discriminable.

Background radiation can produce nuclear recoils—caused by alphas and neutrons—and electronic recoils—caused by betas and gammas. The main source of these backgrounds, excluding beta decays, can be traced to primordial radioisotopes and their decay chains both in the environment (*i.e.* the rock walls surrounding SNOLAB) and in the detector materials themselves. Primordial radioisotopes are radioactive elements that have existed since the formation of the Earth, with mean decay lifetimes $\gtrsim 10^9$ years [17]. The most significant of these for DEAP-3600 are ^{232}Th , ^{238}U and their progeny and, to a lesser extent, ^{40}K . Both ^{238}U and ^{232}Th produce alphas, betas and gammas during their decays, and the energies of the emitted particles along with the full decay chains can be seen in Figures 2.4 and 2.5.

Mitigation of these backgrounds was performed through both detector design and construction, as well as through analysis. DEAP-3600 was designed and constructed to have less than 0.6 background events in a 3000 kg-yr exposure [30]. This section will discuss each of the aforementioned types of background radiation, their sources, how they were constrained during commissioning, how they are dealt with analytically and their potential to mimic a WIMP signal.

2.3.1 Alpha Particles

The primary source of alpha decays in DEAP-3600 come from ^{222}Rn , ^{220}Rn and their daughters (shown in Figures 2.4 and 2.5) in the bulk materials, and from ^{210}Pb on the inner AV surface [31]. Radon contamination can arise from impurities in the detector materials and the ambient air in underground labs. Strict material selection was employed to choose radiopure materials and stringent monitoring of the production of the acrylic and TPB was

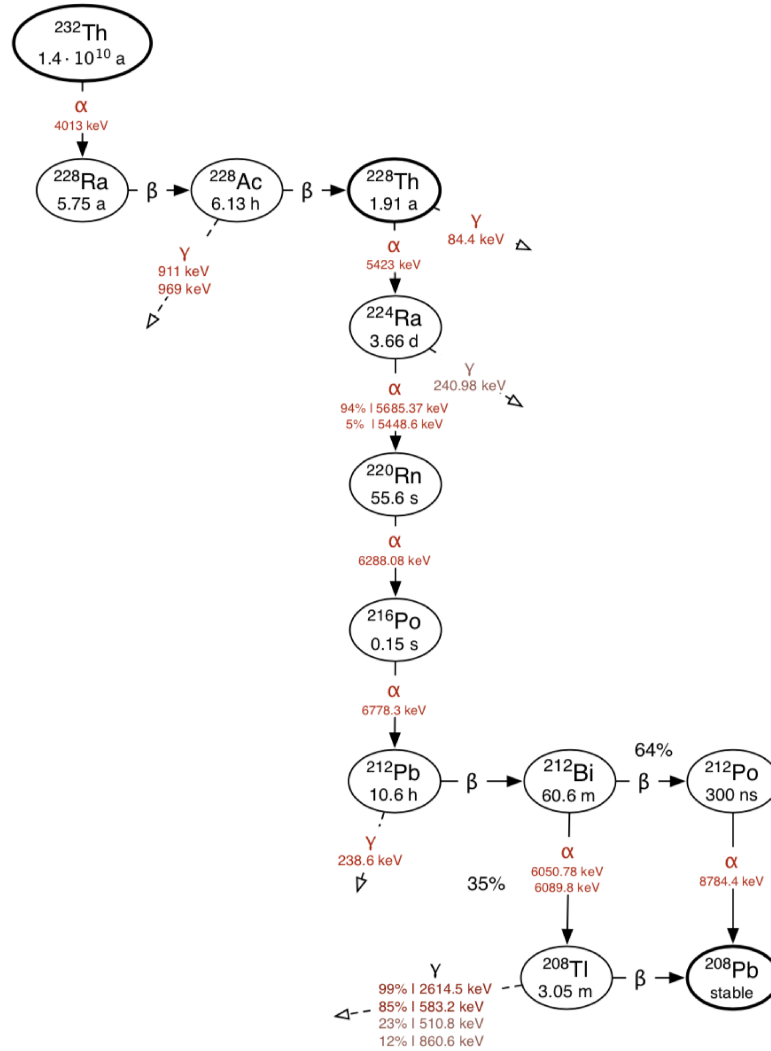


Figure 2.4: Decay chain of primordial ^{232}Th [38]. The times denote the elements' half lives. Branching ratios of less than 1% are not shown.

performed to ensure their radiopurity. Cryogenic purification of the argon removes radon before it is introduced to the AV [31].

Airborne radon contamination stems from radon gas produced in the decay chains of ^{232}Th and ^{238}U within the rock and is a dominant source of radioactivity in underground labs [17]. While the acrylic pieces of the AV were produced at the surface, final construction occurred underground at SNOLAB, where the AV was exposed to air with ^{222}Rn levels of $\approx 130 \text{ Bq/m}^3$ [31]. Once it was completed, but prior to the TPB deposition, a resurfacer was inserted via the neck into the AV to remove 0.5 mm of the inner surface of the acrylic [30]. This was done because ^{222}Rn decays into ^{218}Po and ^{214}Po , that can ionize and adhere to solid surfaces like the AV, where it will further decay into ^{210}Pb [38]. Additionally, the

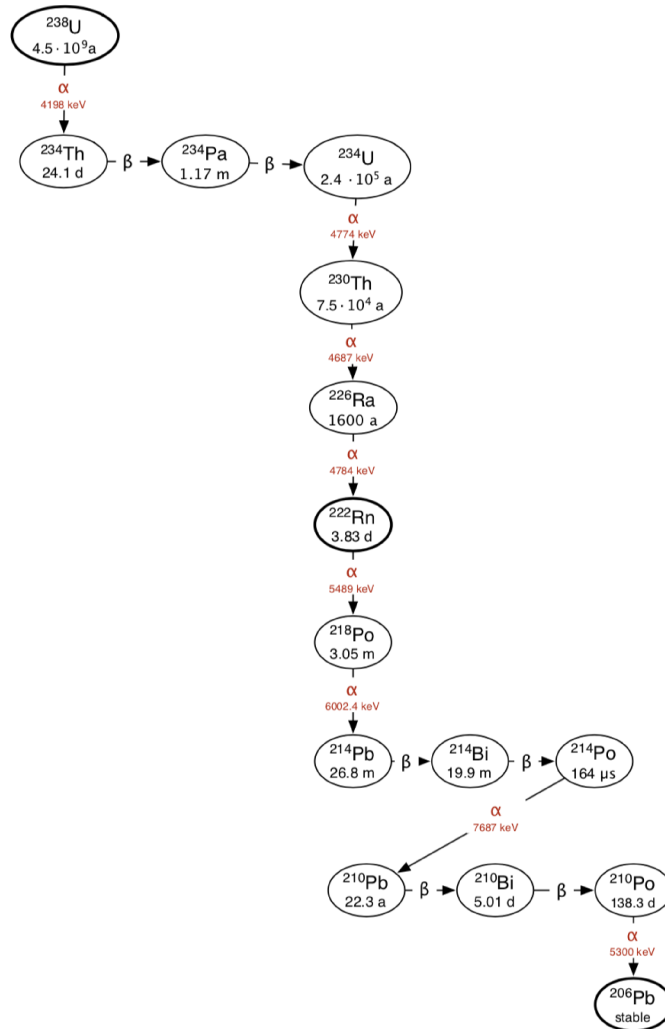


Figure 2.5: Decay chain of primordial ^{238}U [38]. The times denote the elements' half lives. Branching ratios of less than 1% are not shown.

radon-scrubbed nitrogen gas that purges the steel shell, discussed in Section 2.2.3, serves to shield the inner detector from ambient radon [17].

Typical alpha decays are not a background concern despite causing nuclear recoils as they have much higher energy than potential WIMP signals. However, they can leak into the ROI if they lose some of their energy prior to reaching the bulk LAr. This can happen in two ways. The alpha can first scintillate in Ar in the neck and then scintillate in the bulk LAr, or the alpha decay can occur on a surface, depositing some of its energy into that material before scintillating in the bulk LAr [30]. Neck alpha scintillation can occur due to small pockets of LAr that gather in areas of the neck, such as on parts of the cooling coil and flow guides. Surface alpha decays come from residual ^{210}Pb on the AV decaying into ^{210}Po which then emits alphas. These alpha decays occur in either the first 80 μm of acrylic, or at

the interface between the AV and TPB, before they enter the bulk LAr where they deposit the remainder of their energy [30]. The ROI signals due to alphas initially scintillating in the neck can be removed using the neck veto and the top2ringsfrac cut described in Section 2.2.4. A radial fiducial volume cut is used to remove events that occur due to surface alpha decays [30].

2.3.2 Neutrons

Background radiation from neutrons entering the detector may recoil off of an ^{40}Ar nuclei, mimicking a WIMP recoil if it has sufficient energy deposition [30]. There are three sources of neutrons in DEAP-3600: cosmic ray muons and primordial radioisotopes in the rock wall and in the detector materials. Cosmic rays create showers of secondary particles when going through the Earth's atmosphere and, at sea level, the resultant muon flux is around $14.4 \times 10^6 \text{ m}^{-2}\text{day}^{-1}$ [35]. Locating DEAP-3600 underground at SNOLAB provides a 6000 meter water equivalent overburden that decreases the cosmic ray muon flux to $0.27 \text{ m}^{-2}\text{day}^{-1}$. Cosmic ray muons are tagged by the muon veto discussed in Section 2.2.3, which is used to reject both the fast and slow cosmogenic neutrons they can produce via spallation in the detector materials [31, 17].

The main source of neutrons comes from primordial radioisotopes in the rock and the borosilicate PMT glass, which can produce neutrons in two ways. Energetic neutrons can be produced by alpha particles emitted from the decays of ^{238}U and ^{232}Th undergoing (α, n) reactions. During this process, the alphas are absorbed by nuclei, prompting the emission of fast neutrons [38]. The other, much rarer, contribution is via spontaneous fission of these elements. The water tank sufficiently shields the detector from these neutrons that originate in the rock [31]. The dominant source of neutrons ($\sim 70\%$ of them) are from (α, n) reactions in the PMT glass [30]. These are mitigated by the acrylic LGs and the filler blocks, both of which moderate neutrons. Within the half meter of shielding, the neutrons are thermalized, sufficiently lowering their energies such that they either undergo neutron capture before reaching the LAr or their probability of producing a false WIMP signal is very low [39]. Work performed to constrain the in-situ neutron flux by searching for coincidences between a nuclear recoil and the subsequent gamma ray interaction from the neutron being captured by either ^{40}Ar or ^1H is underway [30].

2.3.3 Beta Decays and Gamma Rays

Both beta decays and gamma rays populate the electronic recoil band, highlighted in Figure 2.1. These interactions stem primarily from intrinsic isotopes of the LAr in the detector

volume and from primordial radioisotopes in the detector components. The dominant source of beta decays originate directly from the LAr, specifically the isotope ^{39}Ar . This is an intrinsic cosmogenic isotope found in LAr produced from atmospheric gas, with an activity of 1.01 ± 0.10 Bq/kg [40]. Recoils from the beta decays are the main contributor to the low energy events within the ER band. The second intrinsic isotope of ^{40}Ar that causes background radiation is ^{42}Ar , which beta decays to ^{42}K and subsequently beta decays into either the ground state or an excited state of ^{42}Ca ; producing a gamma ray when it de-excites to its ground state [41]. These interactions contribute to the high energy (≥ 2.6 MeV) events of the ER band [30]. The main source of gamma rays in the detector are the primordial radioisotopes (^{232}Th , ^{238}U , and ^{40}K chains) in the PMT glass. Most of these radioisotopes produce events with energies between 0.5 and 2.6 MeV [30], though gammas from ^{208}Tl (a daughter of ^{232}Th) have energies slightly above 2.6 (as shown in Figure 2.4) and thus also contribute to the high energy events in the ER band.

Electronic recoils create predominantly triplet state excimers that decay more slowly than singlet state excimers, placing the ER band at a lower F_{prompt} than the NR band where WIMP recoils would generally occur [30]. Pulse shape discrimination is used to distinguish between ER and NR in the WIMP energy region of interest, with a 90% acceptance rate and less than 1.2×10^{-7} measured leakage probability [10]. Beyond this leakage, high energy electromagnetic interactions have a chance of entering the ROI if they deposit some of their energy first in the acrylic before scintillating in the LAr. The possibility of this, in the case of the 2614.53 keV gammas coming from the PMT glass, is discussed in Chapter 4.

Chapter 3

Energy Resolution

The energy resolution is the detector's ability to accurately distinguish the energy of incoming radiation [42]. It measures how much the detected energy fluctuates in response to the same energy deposition [35]. Smaller fluctuations indicate better ability to differentiate events, leading to higher confidence in particle identification. Therefore, knowing the energy resolution of the detector is essential in characterizing the detector's behavior. Gamma lines are used in calibrating the energy resolution of the DEAP-3600 detector because they have discrete energy levels over a wide range of energies. This chapter will discuss studies of the DEAP-3600 measured energy resolution with gamma lines using in-situ data and compared to simulations.

3.1 Measured Gamma Ray Energy Resolution

Prior to this study, the energy resolution of the DEAP-3600 detector had only been investigated using the energy per event (event qPE) calculated by the charge processing algorithm. The event qPE was calculated using pulse and subpeak level variables, explained below, over a restricted time window and was corrected for the individual PMT and PMT channel gains. This section explores the energy resolution starting from the raw charge of the event and then correcting for gain and relative efficiencies to determine how much these factors improve the resolution.

A single data run (18024) was analyzed for this study (a run being a period of constant data taking). Sufficient statistics from this single run make it possible to observe the effect on the resolution. The data run (livetime 23 hours, 6 minutes and 48.483 seconds) met the requirements of satisfying the physics trigger and occurring in a stable period during the LAr filling phase of the detector (taken over August 7, 2016 to August 8, 2016). During the run, the LAr level was at a constant height of 590 ± 50 mm above the equator of the AV,

Table 3.1: The series of cuts applied to clean the run data, with a focus on removing events that could artificially broaden the energy resolution. The technical cut includes the variable name used in the DEAP data structure and the value used to exclude events from the analysis. Information on the cut values and descriptions are from [43, 44].

Cut Category	Description of Event Cut	Technical Cut and Value (An event is skipped if:)
Data Quality	flagged as internal periodic trigger or external calibration trigger	dtmTrigSrc & 0x82
	instances of poor DAQ or detector behavior	calcut & 0x31f8
Event Quality	pile up of coincidence events (two interactions in the same time window)	subeventN != 1
	pile up caused before the primary interaction	trigTime <= 2350
	pile up caused after the primary interaction	trigTime >= 2650
	significant amount of early light	numEarlyPulses >3
	pile up from previous events	deltat <= 20000
	almost all of the charge is in the last half of the event	frontHalfFraction >0.98
	LG Cherenkov and high F_{prompt} afterpulsing	fmaxpe >0.2

corresponding to a LAr mass of 3322 ± 110 kg [10]. The data that were analyzed here are a subset of the total run known as a skim file. The file is created by performing cuts on the data that isolate specific types of events, such as gammas or alphas, and adding them to separate files for an optimized analysis. To skim the gamma events, cuts on the data kept events with an F_{prompt} between 0.2 and 0.4 and an event qPE greater than 6000 PE. Default cuts, defined by the collaboration to clean the data, were also applied and are listed in Table 3.1.

As mentioned in Section 2.2.2, calibration and analysis processors are run over the raw data, which has the detected light stored as digital waveforms, with charge and time in units of ADC and ns, respectively. One of these processors, *smartcal*, is responsible for extracting pulses from the PMT waveforms and converting them from ADC units to picoCoulombs (pC). *Smartcal* scans through the waveforms and extracts the pulses, that are identified by the waveform passing the threshold value of 5 ADC below the baseline of 3900 ADC (see Figure 3.1 for an example of an SPE pulse) [45, 31]. There can be multiple peaks within each pulse—referred to as subpeaks—and the charge and timing information are extracted for each. The charge and timing are then calibrated and saved in the data structure in units of pC and ns, respectively. Summing the charge of each subpeak in all of the triggered PMTs for an event gives the total charge in pC. This is referred to as the raw charge, but can also be interpreted as the uncalibrated energy of the event. The raw charge was the first low-level variable analyzed for run 18024, and its spectrum is shown in Figure 3.2.

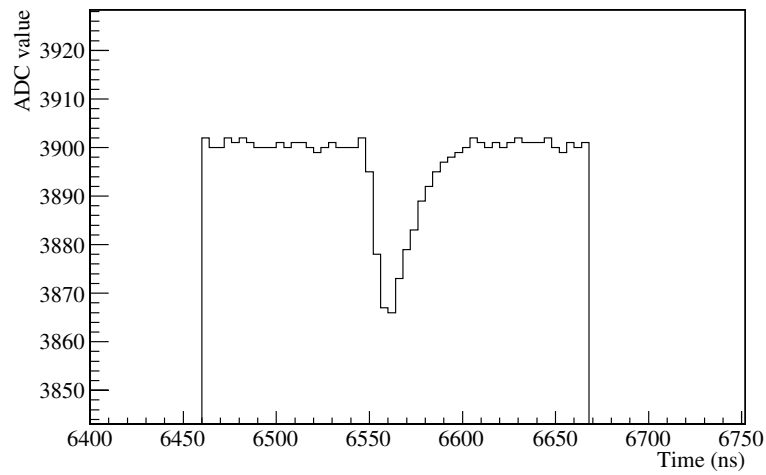


Figure 3.1: Plot showing a measured single photoelectron pulse with a baseline of 3900 ADC [31]. The threshold for pulse identification is 5 ADC below the baseline.

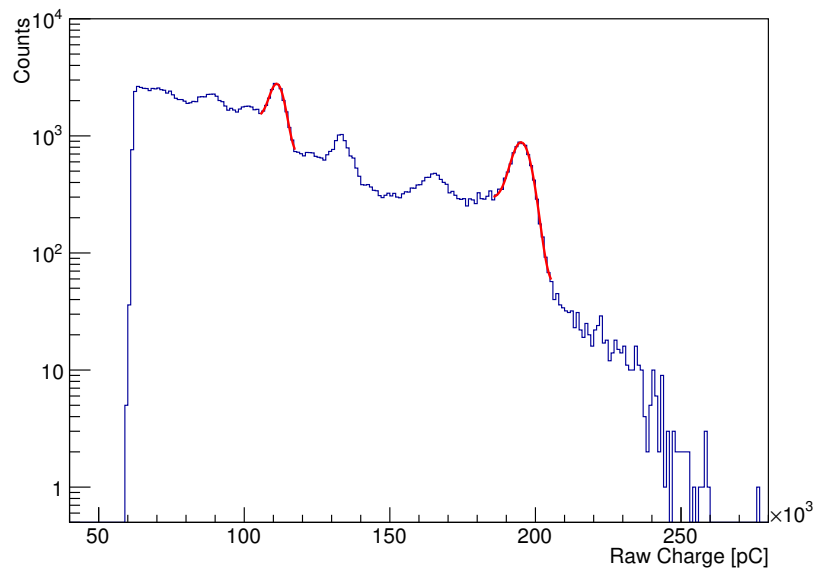


Figure 3.2: The raw charge spectrum (blue) of the gamma interactions for run 18024. The red lines show fits to the peaks using Eqn. 3.4. The spectrum has 1000 pC binning.

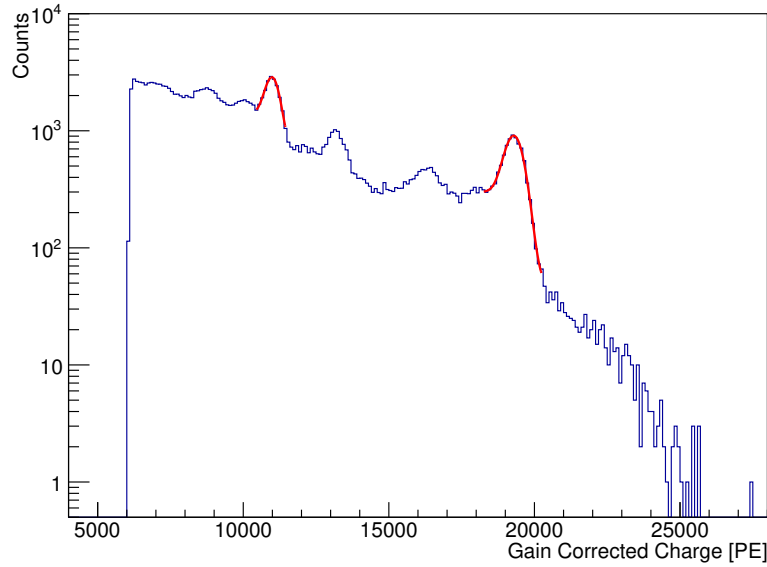


Figure 3.3: The gain corrected charge spectrum (blue) of the gamma interactions for run 18024. The gain corrected charge was calculated for each event using Equation (3.1). The red lines show fits to the peaks using Equation (3.4). The spectrum has 100 PE binning.

A spectrum for the gain corrected charge was subsequently created. The gain correction accounts for both the PMT gain and any amplification that occurs in the PMT channel (the electronics chain connected to each PMT, including the SCBs, etc.). The term "relative channel gain" is used to encompass both the PMT gain and the amplification from the PMT channel. A fit to the charge distribution for each PMT is used to determine the relative channel gain. This charge response function gives the average charge (in pC) that is produced from a single photoelectron (SPE) being emitted from the photocathode [34]. The gain correction was implemented using Equation (3.1):

$$C_{gain} = \sum_{i=0}^{254} \frac{Q_{i,raw}}{Q_{i,SPE}}, \quad (3.1)$$

where i represents the PMT being summed, $Q_{i,raw}$ is the raw charge of the PMT, $Q_{i,SPE}$ is the SPE charge of the PMT and C_{gain} is the gain corrected charge of the event. This produces an energy spectrum in units of PE, shown in Figure 3.3, referred to as the gain corrected charge. Correcting for each relative channel gain accounts for fluctuations in the response of individual channels.

An additional method of ensuring uniformity in the behavior of the PMTs is to apply data from one of the dedicated optical calibration methods, *e.g.* the laserball. The laserball is a nearly isotropic light source that was inserted into the AV before it was filled with LAr.

It is used to characterize both the timing of the inward facing PMTs [34] and the relative efficiencies of the PMTs and channels. The relative efficiency is the number of measured pulses from the PMT divided by the relative number of photons that strike the PMT. This correction was applied to the raw charge in two ways: as a singular correction, and in combination with the gain correction, as shown in Equations (3.2) and (3.3), respectively:

$$C_{eff} = \sum_{i=0}^{254} \frac{Q_{i,raw}}{L_{i,eff}}, \quad (3.2)$$

$$C_{gain,eff} = \sum_{i=0}^{254} \frac{Q_{i,raw}}{Q_{i,SPE} \times L_{i,eff}}, \quad (3.3)$$

where i , $Q_{i,raw}$ and $Q_{i,SPE}$ are the same as above, L_{eff} is the relative efficiency of the PMT, C_{eff} is the relative efficiency corrected raw charge of the event (in pC) and $C_{gain,eff}$ is the gain and relative efficiency corrected charge of the event (in PE).

Figure 3.4 shows the charge spectrum corrected for relative efficiencies, where one may directly compare the effect on the energy resolution of correcting for the gain versus the relative efficiency. Figure 3.5 shows the spectrum when the relative efficiency correction was applied in addition to the gain correction. Applying both corrections to the raw charge accounts for both intrinsic behavioral differences between the PMTs and the variation in the PMT response to uniform light emitted at different locations within the detector.

As a baseline, in order to compare the performance of the various types of corrected charge spectra, the event qPE gamma spectrum was created (see Figure 3.6).

With these different spectra in hand, the next step was to determine the energy resolution. There are four distinct peaks in Figures 3.2 to 3.6. From left to right the peaks represent the 1460 keV line of ^{40}K , the 1764.5 keV and 2204.1 keV lines of ^{214}Bi and the 2614.5 keV line of ^{208}Tl [46]. The outer two distinct peaks were chosen to be fit individually. The two ^{214}Bi peaks were not fit due to contributions from other neighboring ^{214}Bi gamma lines widening the peaks and creating double peak features [43]. With multiple gamma lines contributing to the spectrum, along with the Compton continuum, the peaks are not fully Gaussian. To account for this, each peak is fit with the function in Equation (3.4); a combination of a constant, a Gaussian cumulative distribution function (CDF) and a Gaussian function [43]:

$$L - \frac{L - R}{\sqrt{2\pi}\sigma} \int_{-\infty}^x e^{-\frac{(x'-\mu)^2}{2\sigma^2}} dx' + A e^{-\frac{1}{2}\left(\frac{x-\mu}{\sigma}\right)^2}. \quad (3.4)$$

Here L and R are the average background below and above the peak energy, σ is the standard deviation of the detected energy, μ is the average measured energy, and A is the background subtracted amplitude of the peak energy. The starting values of the fit are chosen from

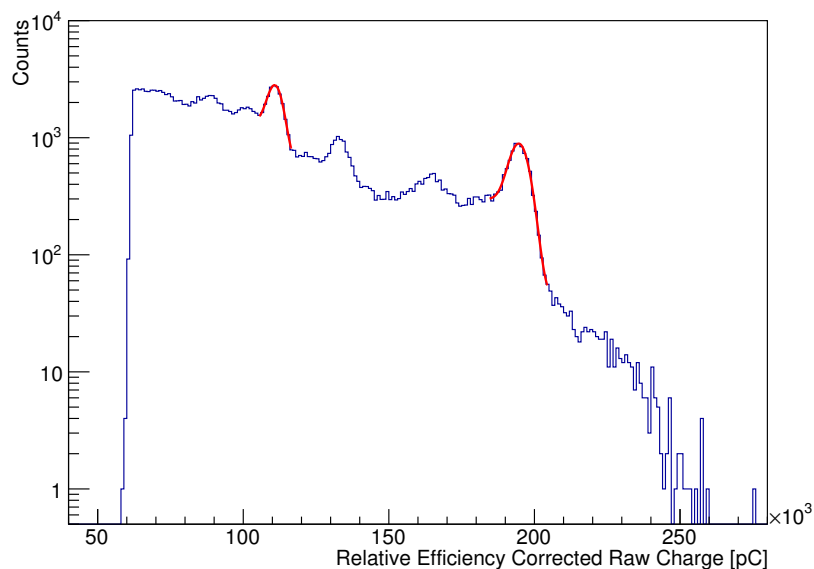


Figure 3.4: The raw charge gamma spectrum (blue) for run 18024 after correcting for the relative efficiencies obtained from the laserball data. The relative efficiency corrections were applied using Equation (3.2). The red lines show fits to the peaks using Equation (3.4). The spectrum has 1000 pC binning.

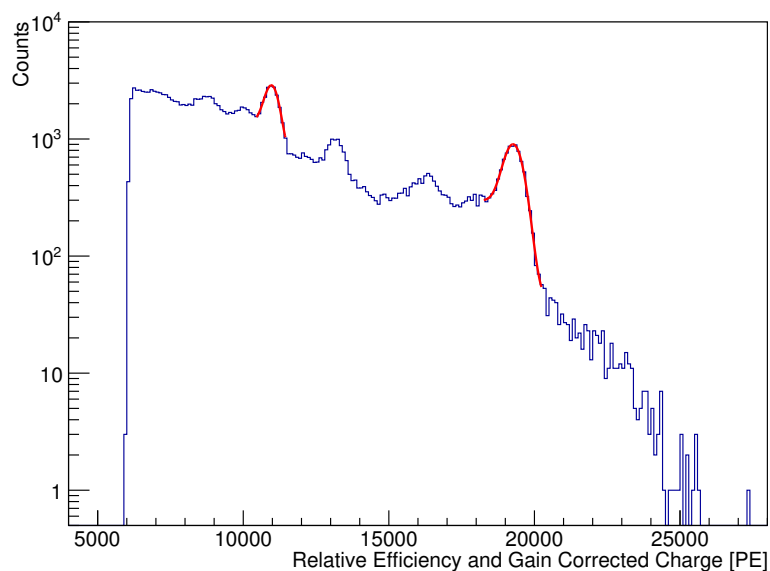


Figure 3.5: The measured gamma spectrum (blue) corrected for both the relative channel gain and the relative efficiency. The corrections were implemented on the raw charge with Equation (3.3). The red lines show fits to the peaks using Equation (3.4). The spectrum has 100 PE binning.

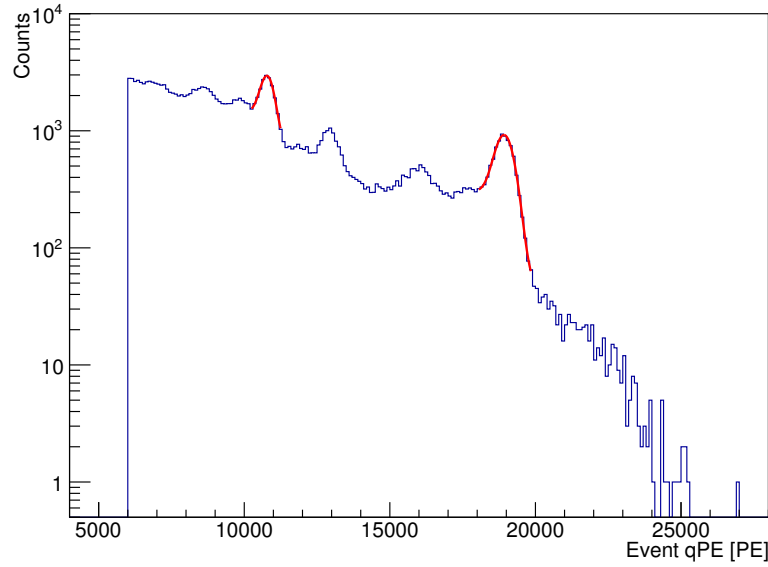


Figure 3.6: The gamma spectrum (blue) created using the event qPE calculated by the DEAP charge processor. The red lines show fits to the peaks using Equation (3.4). The spectrum has 100 PE binning.

each plot (see Figure 3.7b). The local minima between peaks is calculated. If that value is closer to the mean than 5% above or below μ , then it is chosen as the edge of the fit range, otherwise, the edge of the fit range is set at 5% above and/or below the average measured energy. The initial value of σ is half of the range and the number of events at each edge of the range is input for L and R . The starting value for μ is determined by a ROOT tool called TSpectrum that identifies the positions of peak candidates in a spectrum. The initial input amplitude is the number of events with energy μ minus the average background below the peak. A chi square function is used to fit Equation (3.4) to each peak with an input uncertainty of \sqrt{N} , where N is the number of events in each histogram bin.

The mean, sigma and their associated uncertainties are extracted from the fit and used to calculate the energy resolution and its uncertainty. As the probabilities in Table 3.2 show that the fits are consistent with Equation (3.4), the energy resolution is defined as the full width half maximum (FWHM) of a peak, divided by its mean and multiplied by 100, shown in Equation (3.5), where μ and σ are extracted from the fit of Equation (3.4). The energy resolutions of the ^{40}K and ^{208}Tl peaks for each spectrum are listed in Table 3.1.

$$\text{Energy Resolution} = \frac{\text{FWHM}}{\mu} \times 100 = \frac{2.35\sigma}{\mu} \times 100 \quad (3.5)$$

Comparing the values in Table 3.3, it is apparent that there is no significant difference in

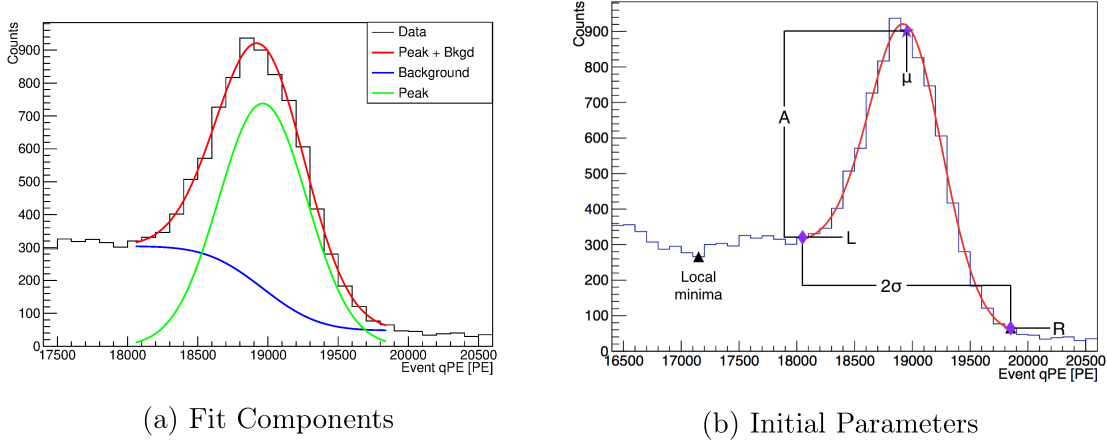


Figure 3.7: Plots of the ^{208}Tl peak and fit for the event qPE gamma spectrum. (a) The components of the Equation (3.4) plotted individually along with the full fit. The background is the constant with the Gaussian CDF and the peak is the Gaussian function. (b) Visual aid of the initial parameters input for fitting each peak with Equation (3.4). Purple diamonds indicate the edges of the fit range, while black triangles indicate the unused range values (in this case, the upper range value is the same for both methods).

the energy resolutions for the five spectra. All of the corrected energy resolutions (including event qPE) are within uncertainty of the energy resolution of the raw charge. The greatest improvements are a lessening of the energy resolution by $0.17 \pm 0.27\%$ and $0.08 \pm 0.13\%$ for ^{40}K and ^{208}Tl , respectively. These results mean that the gain and the relative efficiency account for a negligible amount of the energy resolution, indicating that something other than PMT corrections dominate the energy resolution.

It should be noted that the slight discrepancy between the gain corrected charge and the event qPE is due to the time window used for event qPE although the disagreement is not substantial enough to indicate an error in gain correction or charge summation. Since

Table 3.2: The χ^2 value, the number of degrees of freedom (NDF) and the probability of the fits of the ^{40}K and ^{208}Tl peaks.

Gamma Spectra	^{40}K Peak			^{208}Tl Peak		
	χ^2	NDF	Probability	χ^2	NDF	Probability
Raw Charge	7.38	8	0.50	7.92	16	0.95
Gain Corrected Raw Charge	6.26	6	0.40	11.11	16	0.80
Relative Efficiency Corrected Raw Charge	6.70	7	0.46	17.39	16	0.36
Gain & Relative Efficiency Corrected Raw Charge	9.75	6	0.14	13.35	16	0.65
Event qPE	2.94	6	0.82	7.15	14	0.93

Table 3.3: The energy resolution (ER) of the ^{40}K and ^{208}Tl peaks.

Spectrum	ER $_{40K}$ (%)	ER $_{208Tl}$ (%)
Raw Charge	5.11 ± 0.17	3.93 ± 0.09
Gain Corrected Charge	5.14 ± 0.25	3.85 ± 0.09
Relative Efficiency Corrected Raw Charge	5.35 ± 0.21	3.91 ± 0.09
Gain and Relative Efficiency Corrected Charge	5.16 ± 0.24	3.92 ± 0.09
Event qPE	4.94 ± 0.21	3.89 ± 0.10

the PMT corrections displayed insignificant improvement to the energy resolution, the next elements of the study focused on simulations of the gamma rays to test the effect of other potential factors.

3.2 Simulating Gamma Rays in the DEAP-3600 Detector

At this juncture, simulation of gamma ray interactions in the detector allowed for more accurate study of the effect of different factors on the energy resolution. Simulations are a controlled environment where the only interactions will come from gamma rays entering the detector and PMT behavior can be altered to be ideal or mimic reality. Simulations can therefore be used to identify which elements contribute the most to the measured widening of the energy resolution distributions. Specifically, the behavior of the PMTs was analyzed with regards to afterpulsing (AP) since AP is observed to degrade energy resolution in scintillation counting [32].

Afterpulsing occurs within a PMT tube where, in the high vacuum environment (around 10^{-6} to 10^{-5} Pa), some residual gas molecules remain present [32]. Photoelectrons moving through the PMTs may collide with these molecules and ionize them, creating positive ions that are accelerated toward the photocathode. Upon hitting the photocathode, secondary electrons are produced and proceed through the dynode chain as normal. This excess charge will appear as another pulse between a few hundred nanoseconds to a few microseconds after the initial signal pulse [32], increasing the amount of late light. The amount of charge output by an afterpulse depends on the PMT voltage supply, the type of residual gas and where the ion is generated [32]. This means that the same scale afterpulse can come after either a low or high charge signal. This can affect the measured energy resolution in two ways: the pulse may be included as part of the signal event, having more of an effect on lower energy events since the fractional increase will be higher; or it can trigger the detector and be seen as its own event, adding false signal events to the energy distribution. This not only impacts energy resolution but also F_{prompt} by decreasing and flattening the distribution (*i.e.*

for higher late charge, changes in the prompt charge have less effect on F_{prompt}). Due to the fact that afterpulsing is an artifact of PMTs, the only way to fully remove it, and therefore fully quantify its effect on these variables, is through simulations of the detector.

Simulations of the DEAP-3600 detector are created using RAT (Reactor Analysis Tool), which integrates GEANT4, GLG4sim and ROOT into a single framework [47]. Generation and propagation of particles and physics processes throughout the detector are handled by GLG4sim, which is a GEANT4 based Monte Carlo (MC) application designed specifically to simulate scintillation experiments [48]. GEANT4 is primarily used by RAT for its geometries and command interface and ROOT is utilized for data structure, event input/output and offline analysis [49, 47]. DEAP defines the geometry of the detector components within RAT, as well as the behavior of these components. Once events have been generated, they are treated equivalently in their processing to data collected events. Event information and variables created by the processors are written to the data structure and output into ROOT files. For this analysis, the module governing the PMT response was altered for one set of the simulations in order to prevent the creation of afterpulses.

Due to the clarity of the 2.6 MeV ^{208}Tl gamma line in the data (see Section 3.1), it was selected for the simulations for this analysis. The main contributor to this line are gamma rays coming from the borosilicate PMT glass [10]. This process is simulated by having the gamma rays emitted uniformly from within the volume of the PMTs (*i.e.* anything yellow in the inward facing PMTs in Figure 2.2). Each gamma is simulated with an initial energy of 2.61453 MeV (the width of the line is negligible as it is 3.94×10^{-11} MeV [50]) and will be referred to as a PMT gamma from this point forward. The initial simulations were performed with the “full detector” setting, that is, with 3600 kg of LAr in the detector, and the default Monte Carlo trigger settings.

Two sets of simulations were initially performed; one with the typical behavior of the detector, and one where the module governing PMT response was altered in order to prevent the creation of AP. These will be referred to as the "WAP" and "NAP" simulations, respectively. Approximately four million PMT gammas were generated for each simulation. Based on the background assays performed, the activity of ^{208}Tl is 9.12 Bq [51], meaning the simulated datasets are equivalent to about 5.1 days of detector livetime.

The energy distributions of the simulated events were plotted using event qPE, shown in Figure 3.8. Using the same method described in Section 3.1, the 2.6 MeV gamma line was fit and the resultant energy resolutions for WAP and NAP are extracted (see Table 3.4). With the energy resolution lowering by $0.27 \pm 0.03\%$ when AP is removed, this was identified as a much larger effect than the PMT corrections.

The energy resolution for the WAP simulation is $1.03 \pm 0.10\%$ lower than the resolution of

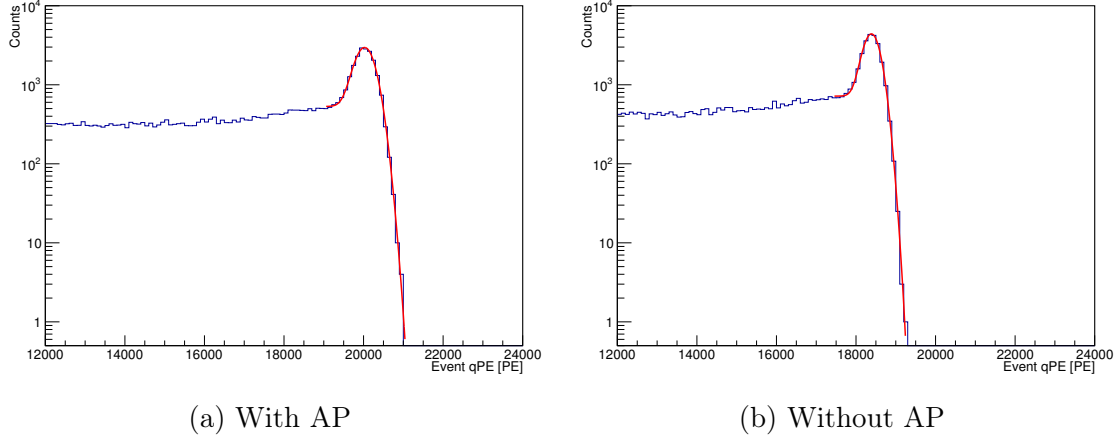


Figure 3.8: The event qPE spectra (blue) for the simulation of PMT gammas (a) with afterpulsing and (b) without afterpulsing. The red line is the fit using Equation (3.4). Plots have 100 PE binning.

Table 3.4: The energy resolution of the PMT gamma event qPE spectra of the ^{208}Tl peak simulated with and without AP.

Simulation	Energy Resolution [%]
With AP	2.86 ± 0.02
No AP	2.59 ± 0.02

the event qPE 2.6 MeV gamma line in data. This could be attributed to a couple of factors: the data are from a physics run and while there are selections to only obtain gamma events, other interactions may be present; the detector is assumed to be perfectly uniform in the simulation; the simulated optics are inconsistent with the optics observed in data; and there are multiple gamma lines contributing to the gamma spectra from data versus the simulation considers only 2.6 MeV gammas.

In addition, concurrent with studying the energy resolution, the effect of AP on F_{prompt} versus event qPE was investigated. Removing the AP decreases the energy and increases F_{prompt} , making the ER band more distinct (see Figure 3.9). This behavior is expected based on the previously discussed effects of afterpulsing. Looking at events below 240 PE (see Figure 3.10), however, some of the events with AP have a noticeably lower F_{prompt} without having an equally noticeable increase in energy. Another unexpected observation was the existence of gamma events in the highlighted region in Figure 3.10, which denotes the WIMP ROI. This prompted the investigations discussed in the following chapter.

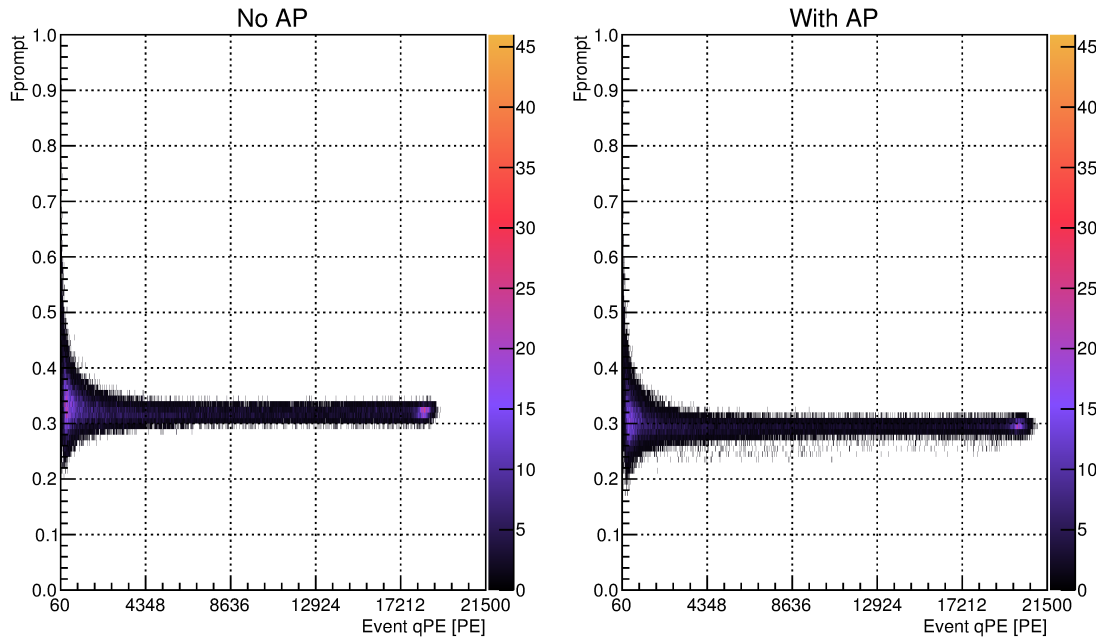


Figure 3.9: Plots of F_{prompt} vs event qPE of the PMT gammas. The plots have single PE binning. The color scale denotes the number of events in each bin. Events below 60 PE are not included in order to see features over the large energy range.

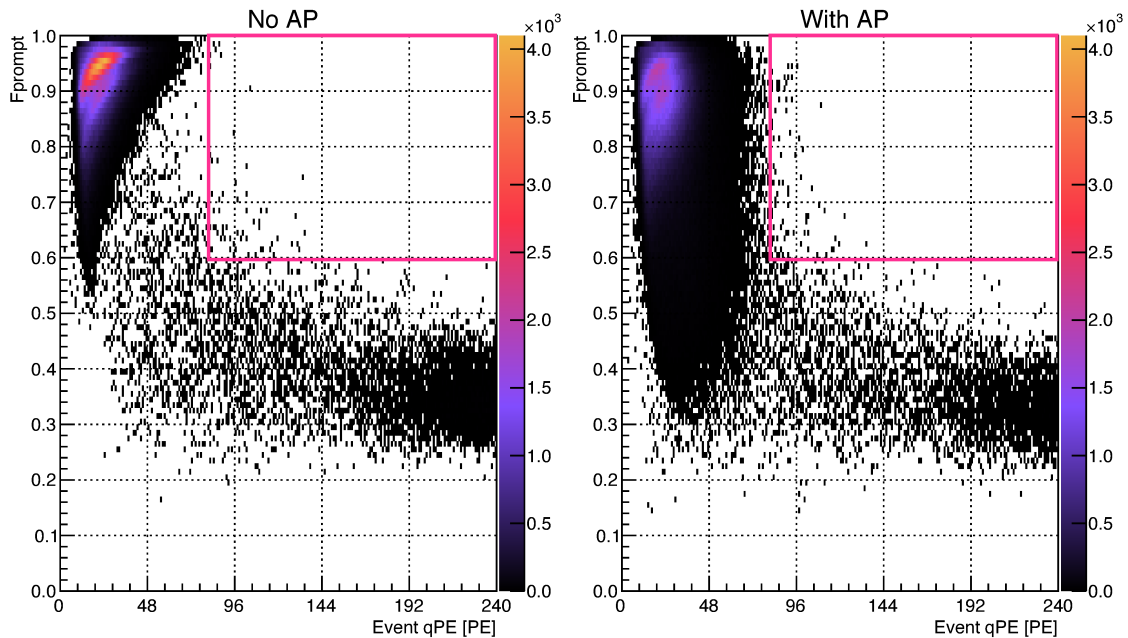


Figure 3.10: Expanded region plots of F_{prompt} vs event qPE, showing the behavior of low-energy events with and without AP. The pink box encompasses the unexpected events observed in the WIMP ROI. The plots have single PE binning. The color scale denotes the number of events in each bin.

Chapter 4

Investigating Gamma Ray Leakage Events in DEAP-3600

Gamma ray events were observed to occur in the WIMP ROI at the end of Chapter 3. This chapter begins by explaining why this observation was unexpected and the decision to study these events. Following that, the mechanism and behavior of these gamma ray events is analyzed and then they are compared to data taken with DEAP-3600. The chapter ends with a discussion of the effect of afterpulsing on these gamma ray events.

4.1 Leakage Events

When evaluating Figure 3.10, it was observed that there were events with the potential to leak into the WIMP analysis region of interest. Figure 4.1 highlights the regions where gamma populations are expected as well as the ROI. Typical gamma events were expected to be either scintillation events—and thus located in the ER band (region (a) in Figure 4.1)—or Cherenkov events—which would have low charge, very high F_{prompt} or both, (placing them in region (b) in Figure 4.1). The events discussed in Figure 3.10 were suspect because they were in neither of these regions and seemed more frequent in the NAP simulation. This implies that a factor other than AP was increasing their charge and decreasing their F_{prompt} , making it possible for them to enter the ROI (labeled as region (c) in Figure 4.1). For the purpose of this study, any simulated gamma events that occur within the ROI ($0.6 < F_{\text{prompt}} < 1.0$ and $80 \text{ PE} < \text{Event qPE} < 240 \text{ PE}$) are referred to as "leakage events". Note that event qPE will be referred to as energy in this chapter unless otherwise specified. The F_{prompt} region of the ROI is chosen to encapsulate the entirety of the NR band and the energy region is chosen to account for the fact that the DEAP simulation does not include fluorescence occurring within the acrylic; this causes the amount of Cherenkov light generated in the simulation to

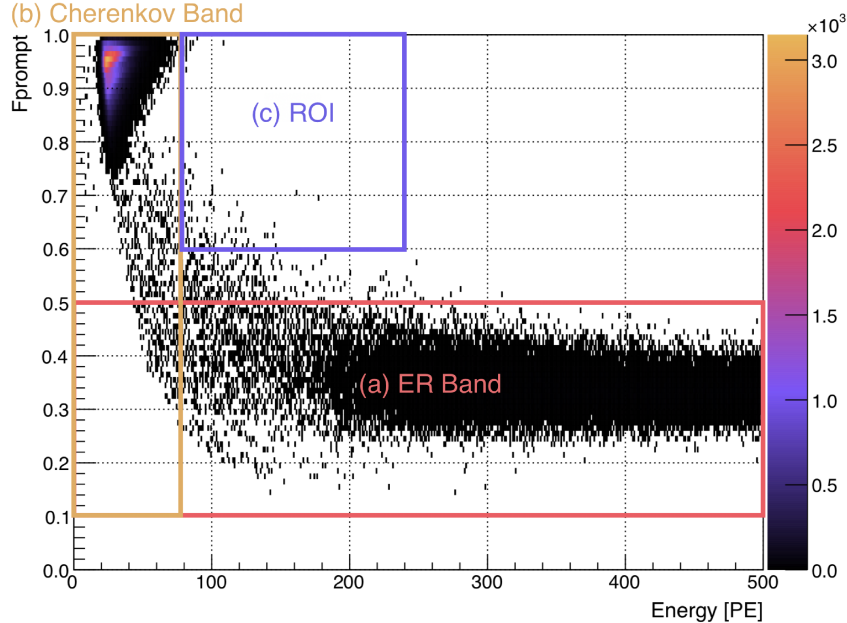


Figure 4.1: Plot of F_{prompt} vs energy for PMT gammas without AP in a partially filled detector. Regions a, b and c denote the electronic recoil band (ER band), Cherenkov band and WIMP region of interest (ROI), respectively.

be less than half the amount of light seen in the data. The goal of investigating the leakage events was to gain a comprehensive understanding in order to isolate them as background events.

4.2 Modifications to the Simulation

To further study the leakage events, the original simulations were modified by altering some of the settings, adding another simulation dataset and saving more of the simulation information to the output ROOT file. The original simulations were created with the geometry for a detector filled with 3600 kg of LAr. However, due to a neck seal failure, it was decided that the detector would only be partially filled to 3300 kg and the geometry in the simulations was adjusted to agree. The fill level was set to a height of 551.0 mm above the equator of the AV, with the remainder of the AV containing gaseous Ar. The other change in the simulated detector settings was the implementation of the detailed physics trigger.

In addition to the NAP and WAP simulations, a third simulation set was created by processing the existing WAP events as if they were data and applying the University of Alberta AP removal method. This simulation set is referred to as "APR". This method removes large afterpulses that cause the waveform to appear to have late pulses. Creating the APR MC allowed for leakage event behavior to be compared for the same physics event,

but with different treatment of the AP. This is not possible when comparing the NAP and WAP simulations. It also made it possible to see how the number of leakage events changed as the amount of AP was decreased.

The last change to the simulations was altering the saved output information in the ROOT files. This had not been done previously because simulations do not automatically save all of the information for each event created in an effort to conserve computing resources. Since the goal here was to investigate the properties of these events that caused leakage into the ROI, it was necessary to have access to all of the information about each event’s path through, and interactions within, the detector. This is done by saving the simulated event tracks; the set of processes that a particle undergoes as it traverses the detector. The processes range from transportation—where the particle moves within the detector without interacting—to interactions with the detector materials. A track ends when the particle has no kinetic energy or a new particle is created by an interaction [47]. Saving this information permitted the analysis of, and comparison between, the interactions of the leakage events.

4.3 Leakage Event Behavior

Figure 4.2 shows the F_{prompt} versus energy distribution in the ROI for the simulations described above. Leakage events are still present, with populations of 88 ± 9 , 73 ± 9 and 107 ± 10 for the NAP, APR and WAP sets, respectively. These simulations represent about 5.1 days of detector livetime.

The tracks of the leakage events were analyzed. This was initially done by evaluating the entire track for a subset of the leakage events from the No AP simulation.¹ The common denominator in all of these events was the presence of a Compton scatter in the acrylic, that deposited at least 0.9 MeV of energy (henceforth referred to as a high-energy Compton scatter), and following scintillation in the LAr. The gamma produced both Cherenkov and scintillation light in its path through the detector. Having established a potential pattern for these events, a script was written to search the tracks of each leakage event for these interactions. A summary of this search can be found in Table 4.1, where most of the high-energy Compton scatters occur in either the AV or LGs, and not all of the leakage events scintillate in the LAr.

Along with the interaction information, each event’s filename, entry number, F_{prompt} and charge were recorded. This revealed that 11 of the APR leakage events had not been WAP leakage events due to the removal of AP that increased the F_{prompt} sufficiently to move the event into the ROI while not decreasing the charge enough to remove it from the ROI.

¹A sample of one of these tracks can be found in Appendix A.

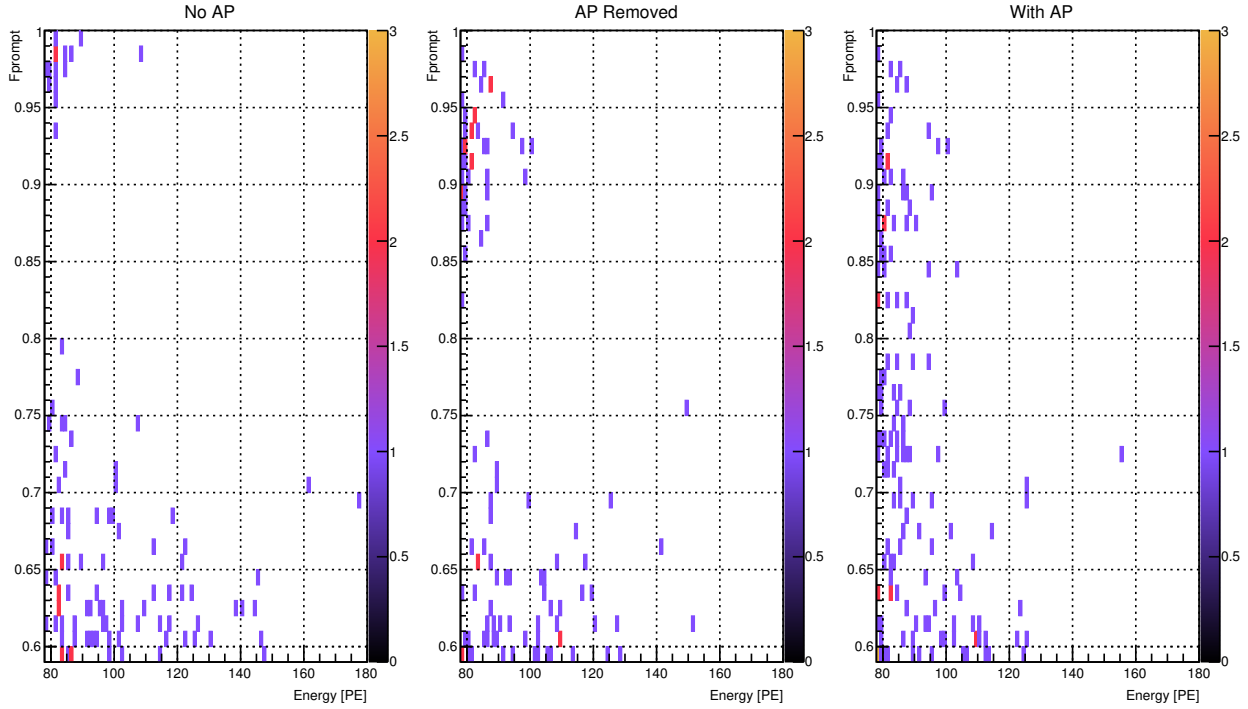


Figure 4.2: Plots of F_{prompt} vs energy of the leakage events for the NAP, APR and WAP simulation data sets. The plots have single PE binning. The color scale denotes the number of events in each bin.

Table 4.1: The number of leakage events for each simulation set along with the number of high-energy Compton scatters and LAr scatters. The information in parantheses is the number of high-energy scatters that occur in each listed location. A total of 11 leakage events in the APR simulation were not leakage events in the WAP simulation.

	No AP	AP Removed	With AP
# of Leakage Events	88	73	107
# of Leakage Events with a High-Energy Compton Scatter	88	73	107
# of High-Energy Compton Scatters and Their Locations	89 (80 acrylic, 6 PMT, 2 filler, 1 LG Finemet magnetic shield)	77 (76 acrylic, 1 PMT)	109 (107 acrylic, 2 PMT)
# of Leakage Events with a LAr Scatter	74	47	36

To further study the interactions shown in Table 4.1, a plot of their locations in cylindrical coordinates (Z vs ρ , centered in the middle of the AV) was created (see Figure 4.3). This should show any biases in position, including if all the high-energy Compton scatters occurred in one region of the detector. It also provides a visual representation of the information in

Table 4.1. No obvious position bias is observed. The lack of high-energy Compton scatters below $\rho = 350$ mm in the upper sphere is expected since the neck attaches to the AV here and there are no PMTs present from which gammas would be generated. The cluster of LAr interactions around $Z \approx 550$ mm is due to the liquid level being at $Z = 551$ mm. None of the scintillation occurs deep within the LAr, as expected for the leakage event gammas that lose most of their energy in the acrylic before reaching the argon. The lack of interactions within the AV above the liquid level is due to the much lower density in the GAr, leading to a much lower probability of interacting. Looking only at the leakage events with scintillation shows no bias in the interaction position. There was also no bias in interaction position found when the events were looked at in the x-y plane.

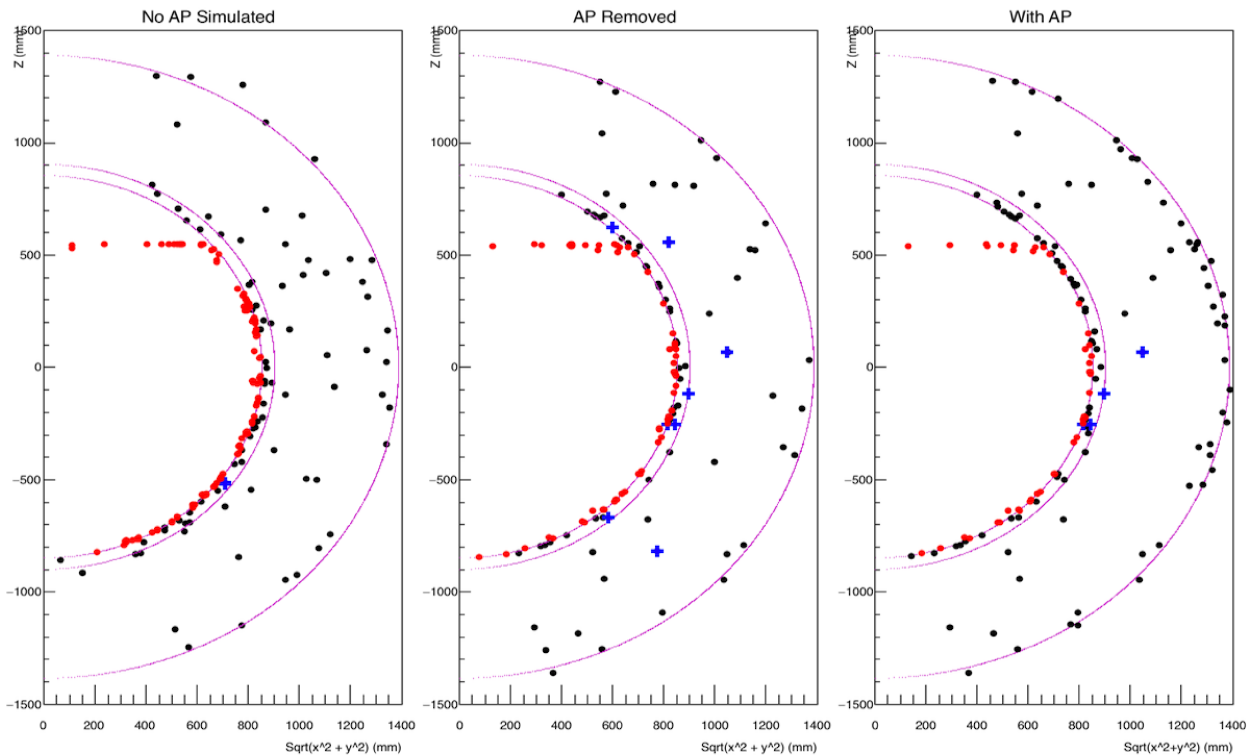


Figure 4.3: Plots providing a visual representation of where the energy is deposited for the interactions listed in Table 4.1. Purple lines denote the AV, LG and PMT radii. Red dots are scintillation events, black dots are high-energy Compton scatters, and blue crosses are events where two high-energy Compton scatters occur.

With the location of the interactions not showing any differentiation between the events with LAr scatters and those without, or providing any evidence of hot spots for Cherenkov light in the inner detector, attention was shifted to the detected distribution of light. This was studied in a couple of ways, both quantitatively and qualitatively, starting with the variable $f_{\max pe}$. $f_{\max pe}$ is the ratio of charge in the highest charge PMT of an event

compared to the total charge for the event. This variable is used to remove Cherenkov light, a common element of all leakage events, as well as high F_{prompt} afterpulsing [52]. The f_{maxpe} distribution is shown in Figure 4.4. The leakage events as a whole have f_{maxpe} values over the full range from 0 to 1. The leakage events with a LAr scatter, shown in the upper plot of Figure 4.4, typically have an f_{maxpe} below 0.35. Comparing both plots in Figure 4.4, however, shows that a some portion of the pure Cherenkov events also have f_{maxpe} below that value. The official cut that DEAP performs is $f_{\text{maxpe}} < 0.2$. Applying this to the leakage events allows only three events without a LAr scatter to remain of the 49, 26 and 21 events that pass the cut for NAP, APR and WAP, respectively. This suggests that the leakage events most likely to remain in the ROI are these with both Cherenkov and scintillation light, prompting further study into these events in particular. This was pursued by qualitatively investigating the overall distribution of light throughout the detector for each event.

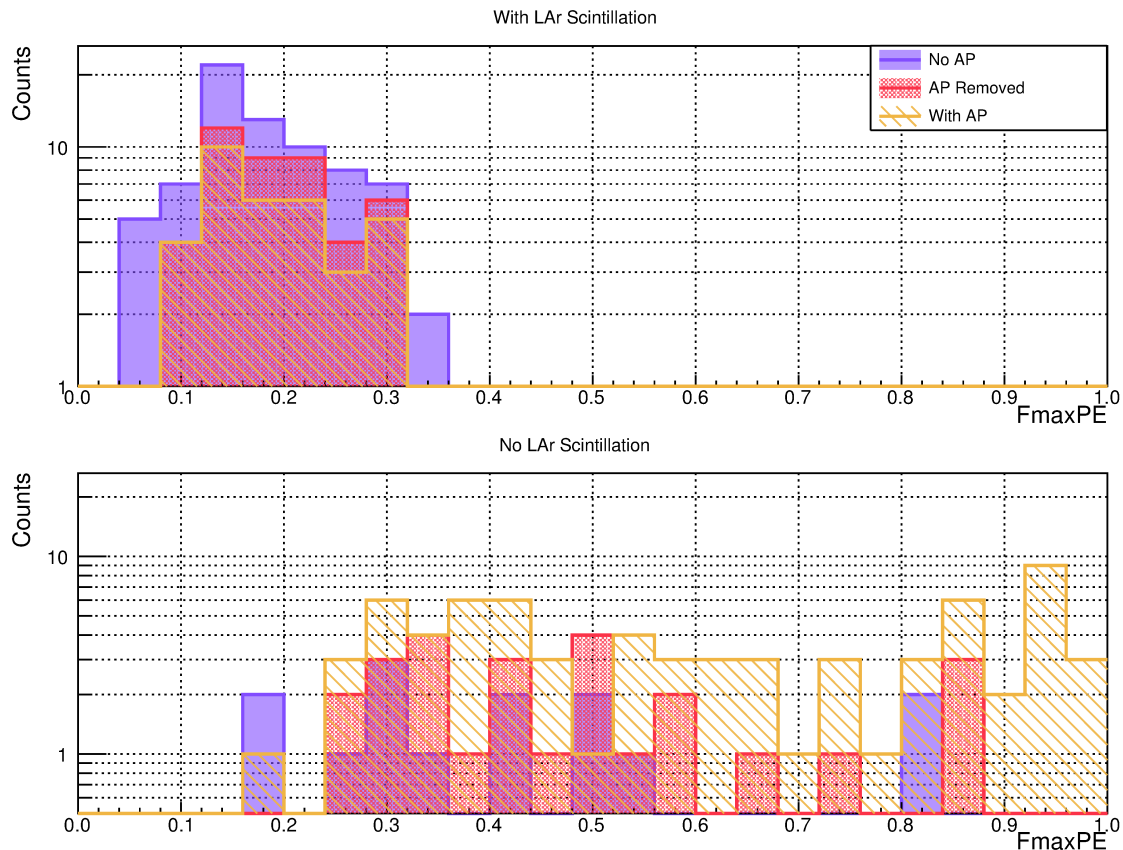


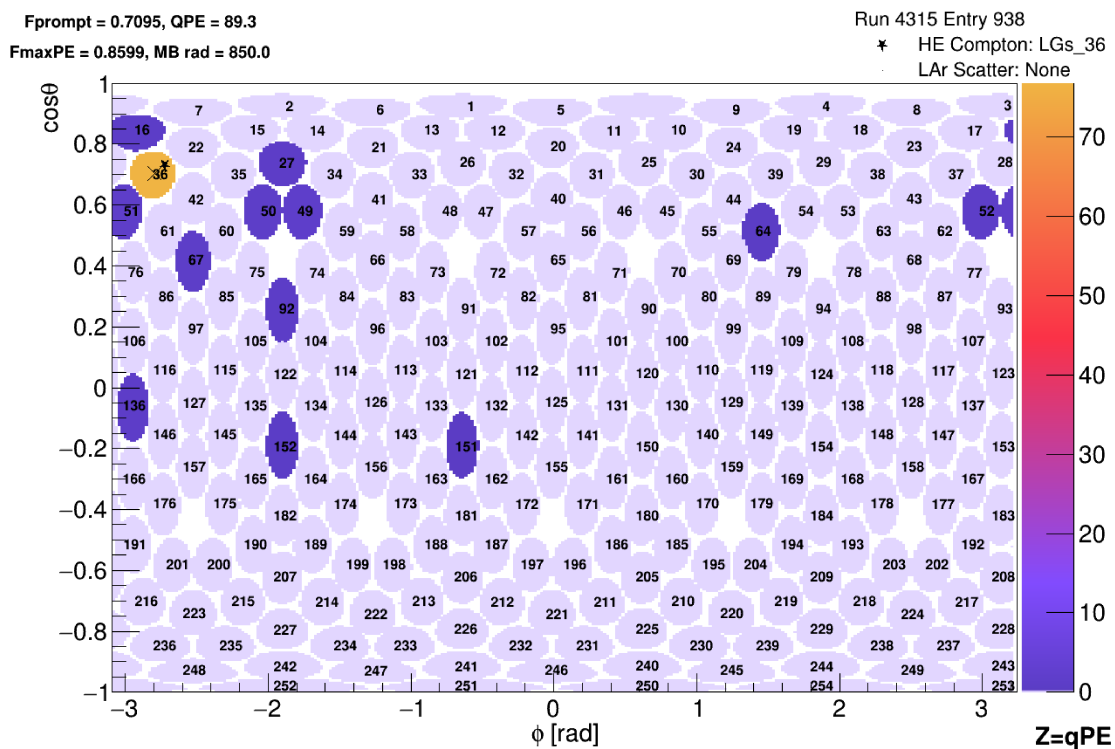
Figure 4.4: Plots showing the distribution for f_{maxpe} for the leakage events of all three simulation sets. The upper plot shows the leakage events that have a LAr interaction while the lower plot contains the leakage events that are purely Cherenkov light. The number of events that pass the f_{maxpe} cut are 49, 26 and 21 for NAP, APR and WAP, respectively. The number of leakage events with a LAr scatter can be found in Table 4.1.

A map of the PMT positions with a color gradient to denote the amount of charge measured at each was created to investigate where the light for each event is detected (see Figure 4.5). PMTs that see no light are colored a very light purple gray to keep the overall layout of the PMTs uniform. The PMT ID numbers are overlaid on their respective PMTs for easier identification/visualization. Different markers are placed on the plot to designate the high-energy Compton scatters and LAr scatters, showing their relation to the PMTs that detected light. It also showed the path of the gamma through the detector and which parts of that path had the most influence on the event charge. An additional marker was placed on the PMT maps to denote where the position fitter, MBfitter, reconstructs the location of the event. This is complementary to the above markers as MBfitter uses the location of the charge detected in the event to determine the event position.

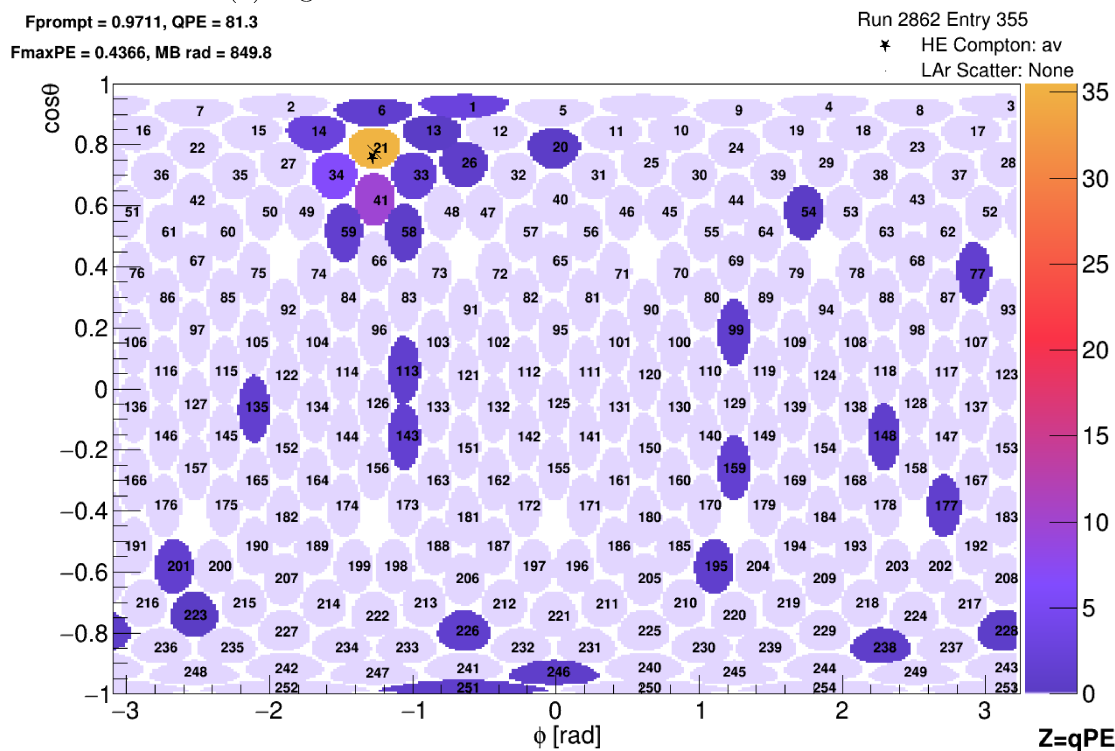
The PMT maps in Figure 4.5 demonstrate the typical appearances of a pure Cherenkov event based on its location in the detector. Figure 4.5a is a plot of an event where the high-energy Compton scatter occurs in Light Guide 36. It can be seen that almost all of the charge for the event is seen by PMT 36, with only a small amount of light reaching other PMTs. The high-energy Compton scatter in Figure 4.5b, however, occurs in the AV. This allows more of the Cherenkov light to reach other PMTs, in particular the neighboring PMTs. This noticeably lowers the f_{maxpe} of the event, though a large fraction of the light is still seen in a single PMT. Both of the events in Figure 4.5 are removed by the f_{maxpe} cut.

The PMT maps shown in Figure 4.6 and Figure 4.7a demonstrate how the distribution of light within the detector changes when the gamma has enough energy to reach the LAr after high-energy Compton scattering. The two figures represent the two primary cases of mixed scattering. Both events pass the f_{maxpe} cut. In Figure 4.6, the gamma travels a ~ 57 cm between Compton scattering and scintillating. In Figure 4.7a, the gamma traverses about a third of that same distance radially within the detector. In Figure 4.6, it can be seen that the Cherenkov light in LG 216 contributes the most, but the existence of the scintillation has consequences: the highest charge PMT no longer detects over a third of the light for the event; the light is much more diffuse than in Figure 4.5, and; there are two distinct sources of light. There is even enough light from the scintillation to shift the fitted position slightly towards the LAr scatter. All of these effects hold true for Figure 4.7a as well, except that without the interactions plotted, this event could look like it came from a single source. Despite the lack of separation, the high amount of diffusion of light allows this event to pass the f_{maxpe} cut. The addition of scintillation distributes the light enough to prevent the event from being identified as a Cherenkov source.

Following this observation, the effectiveness of a different background removal method



(a) Light Guide Cherenkov Event From AP Removed



(b) AV Cherenkov Event From No AP

Figure 4.5: PMT maps showing the distribution of charge for pure Cherenkov events in the LGs or AV. PMTs colored a very light purple gray denote PMTs that did not detect charge. The X marker on the plots denotes the MBfitter reconstructed radius of the event.

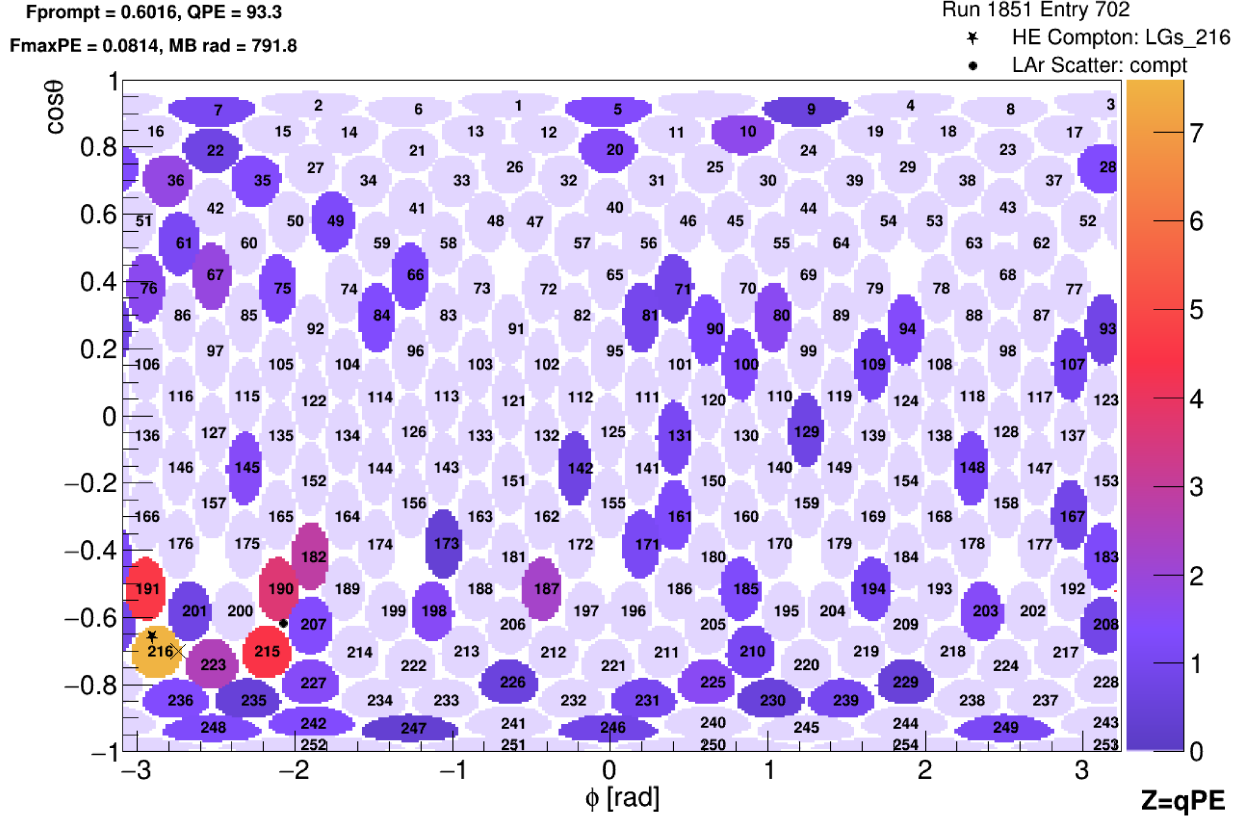
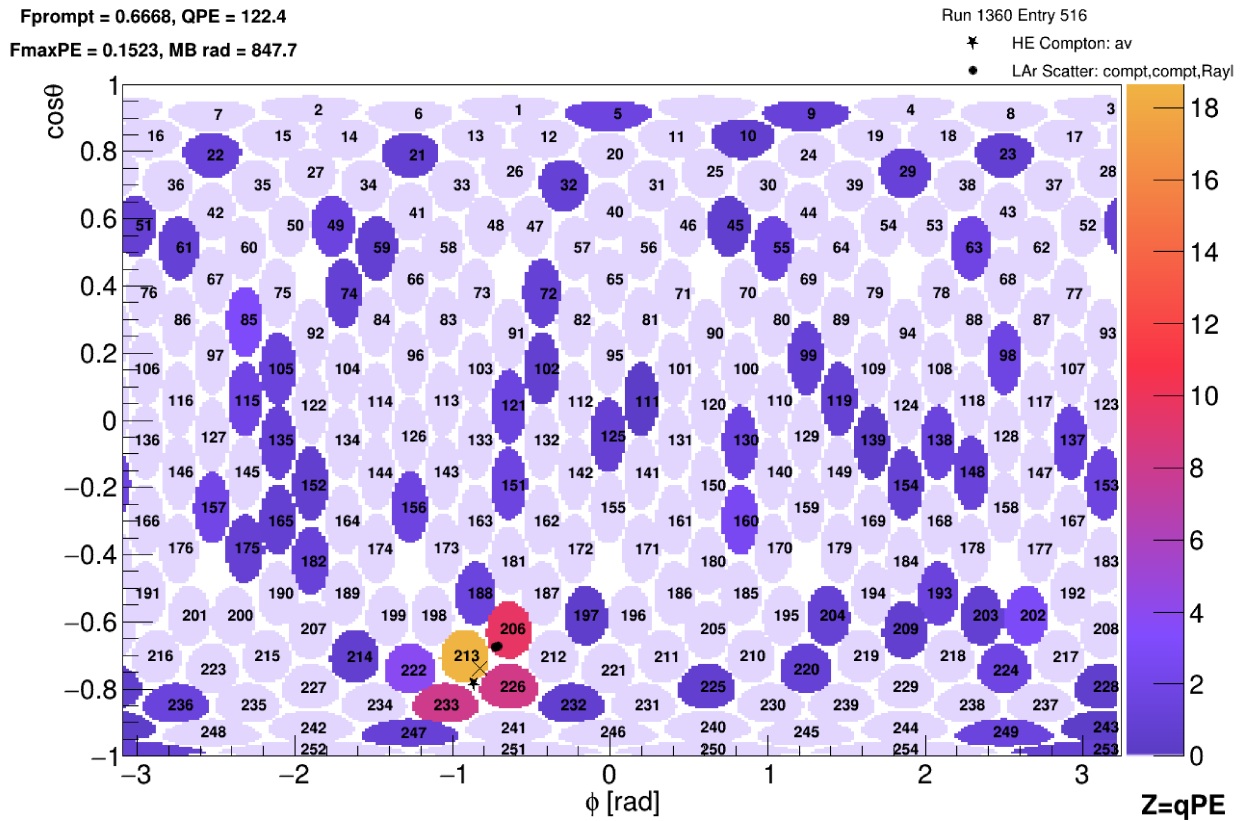


Figure 4.6: PMT map for mixed Cherenkov and scintillation light from No AP. PMTs colored a very light purple gray denote PMTs that did not detect charge. The X marker on the plots denotes the MBfitter reconstructed radius of the event.

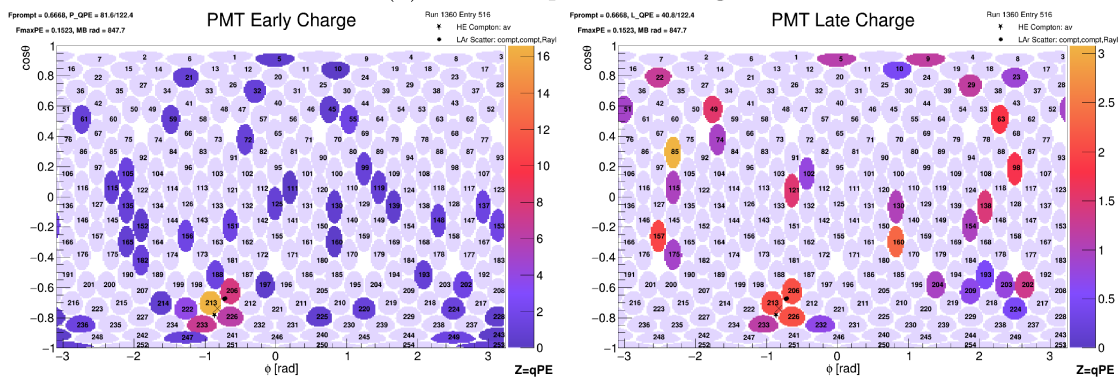
was explored via a data-based processor called *multisite*. *Multisite* identifies events that are a pile up of LAr scintillation and Cherenkov light by examining their prompt timing and/or prompt charge. The latter method, referred to as PromptShiftFrac, finds the local group of PMTs with the highest prompt charge and then examines how much F_{prompt} is changed by removing the prompt light of those PMTs. This is compared to the difference in F_{prompt} that is seen in data for pure Cherenkov and pure scintillation events and the event is cut if it is higher than that value [53]. This removes events such as the one in Figure 4.7. Figure 4.7b shows how much the prompt charge would be affected by removing the charge detected by PMTs 213, 206, 226, 233, 222, 198, and 188—which are the seven PMTs that make up the local group. The other method, known as PromptWidth, is aimed at pile up events in general, finding events where the FWHM of the prompt light pulse is indicative of two events happening close in time due to it being wider than the prompt light pulse of a single event [53].

Despite being designed to remove general pile up, as well as pile up occurring specifically

due to Cherenkov and scintillation happening in the same event, *multisite* does not perform well on the leakage events. It cuts 34, 22 and 31 events for NAP, APR and WAP, respectively, of which 4, 2 and 16 of those events are pure Cherenkov. *Multisite* has been tested on data by combining pure Cherenkov events with pure scintillation events and was able to remove most of those events [53]. Its performance on the leakage events has two possible implications: the simulation is truly that different from the data or that a pile up of both Cherenkov and scintillation from the same gamma is not correctly emulated by combining a pure event of each.



(a) PMT Map Total Charge



(b) Prompt Charge

(c) Late Charge

Figure 4.7: PMT map for a mixed Cherenkov and scintillation light event from No AP (a), along with the PMT maps of prompt (b) and late (c) light. PMTs colored a very light purple gray denote PMTs that did not detect charge. The X marker on the plots denotes the MBfitter reconstructed radius of the event.

4.4 Comparing the DEAP-3600 Detector Simulation to Data

With an understanding of the mechanism causing the leakage events, the next step was to compare the simulation to data taken with DEAP-3600. Specifically, events that were in the ROI and passed a certain set of cuts were evaluated. These events are referred to as "survivor events" to keep a clear distinction between the simulation and data. The survivor events are from data taken between November 2016 and April 2017, which has a livetime of 95.79 days and an exposure of 311,958 kg-days [54]. A series of cuts (listed in Table 4.2) were applied to create the survivor event dataset—similar to the skim files mentioned in Chapter 3.

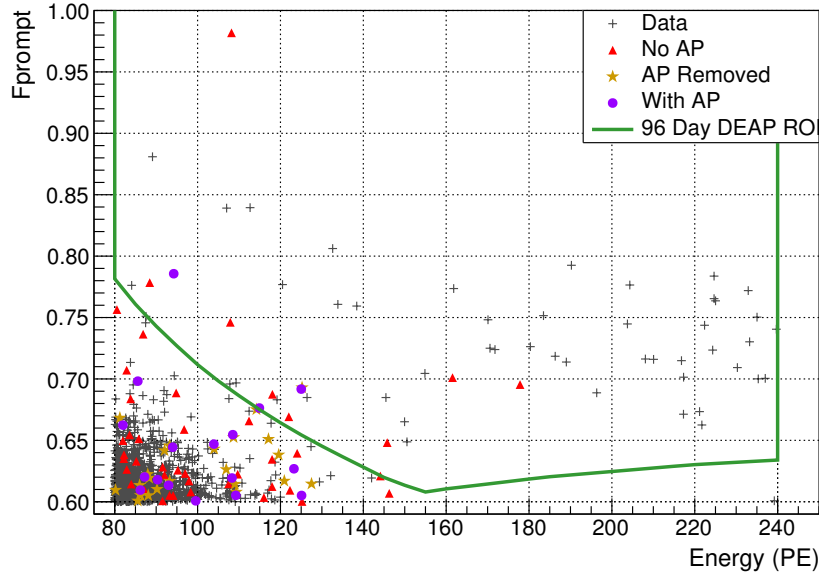


Figure 4.8: Plot showing the leakage events in comparison to the survivor events. Red triangles are simulated events without AP, gold stars are the APR events, purple circles are WAP events and gray crosses are the survivor events. It should be noted that the simulation sets are 1/19 of the livetime of the survivor events and that there are only two cuts applied to the leakage events (to remove the neck events, LG Cherenkov events, and high F_{prompt} afterpulses) while the survivors have the full cut flow applied.

The number of survivor events in the ROI after the cuts are applied is 1105. They are shown in Figure 4.8 as a plot of F_{prompt} vs energy with the leakage events overlaid. As the livetime for the leakage events is ≈ 19 times less than that of the survivor events, fewer cuts (to remove Cherenkov events and neck events) were applied to the leakage events to provide a more visible overlap. The leakage events in Figure 4.8 mainly occupy the lower left region,

Table 4.2: The cuts applied to clean the data, remove known backgrounds and fiducialize the data in order to identify the survivor events. The technical cut includes the variable name used in the DEAP data structure and the value used to exclude events from the analysis. Information on the cut values and descriptions are from [52, 44, 55].

Cut Category	Description of Event Cut	Technical Cut and Value (An event is skipped if:)
Data Quality	no charge information, likely a prescaled event	nspFullW == 0 and qPE == 0
	flagged as internal periodic trigger or external calibration trigger	dtmTrigSrc & 0x82
	instances of poor DAQ or detector behavior	calcut & 0x31f8
Event Quality	bad subpeaks	$1 - \text{nspFullWOverthresh} / \text{nspFullW} > 0.55$ && $\text{qPEfullW} / \text{nspFullW} < 1.20$
	pile up from previous events	$\text{deltat} \leq 20000$ and $\text{precursorCharge} / \text{precursorTime} > 0.0020$ and $\text{precursorNumSubpeaks} / \text{precursorTime} > 0.0015$
	pile up of coincidence events (two interactions in the same time window)	subeventN != 1
	pile up caused before the primary interaction	$\text{trigTime} \leq 2350$ and $\text{timefitT0} \leq 100$
	pile up caused after the primary interaction	$\text{trigTime} \geq 2650$ and $\text{timefitT0} \geq 5500$
	events over too large of a time window to be a single event, basically a check in case the above two fail	eventTime > 15000
	significant amount of early light	numEarlyPulses > 3
	Cherenkov	$\text{nhit} < 100$ && $\text{lateChargePMT} / \text{HadPrompt} / (\text{qPE} * (1 - \text{fprompt})) > 0.75$
	LG Cherenkov and high Fprompt afterpulsing	fmaxpe > 0.2
	events that trigger one of the neck veto PMTs	neckVetoN > 0
Fiducial	surface events based on study of correlation with another pos fitter	mblikelihoodKuiper > 0.25
	surface events based on reconstructed radius from position fitter	TVector3 mbPos(mblikelihoodX, mblikelihoodY, mblikelihoodZ), then mbPos.Mag() >= 800.0
	surface events based on scintillation light	fmaxnsc >= 0.07
	neck events identified by too much charge in the GAR of the AV	$(\text{chargetopring} + \text{chargesecondring}) / \text{qPE} \geq 0.05$

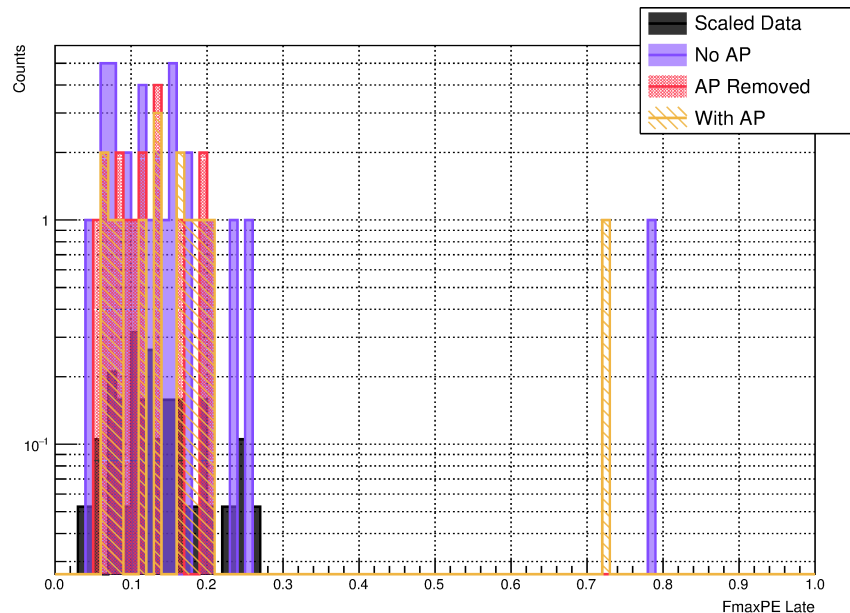


Figure 4.9: The distribution for $f_{\text{maxPE Late}}$ for the leakage events of all three simulation sets as well as for the survivor events (scaled down by a factor of 19 to better match the livetime of the leakage events). Kolmogorov tests between leakage events and survivor events reinforce visual agreement with values of 1 for NAP, APR, and WAP events versus survivor events.

showing that they are a sideband of the ROI. The 96 day DEAP WIMP ROI for the survivor data set is also drawn on the plot, showing that even with the stricter data-based region, some of the leakage events remain present, further demonstrating their likelihood to account for some of the survivor events.

Examining the distribution of the leakage events and survivor events for certain variables also shows some overlap. Variables such as the fraction of charge in the top two rings of the detector, the number of hit PMTs in an event, and the maximum fraction of late light in a single PMT, have significant overlap between the leakage events and the survivors (see Figure 4.9). However, other variables, such as the maximum fraction of light in a single PMT and its nearest neighbors (see Figure 4.10), and the maximum fraction of prompt light in a single PMT, have very little agreement between the two populations.

Overlap in the distributions for some variables between the leakage events and survivor events is significant enough to point to the possibility of the leakage events making up a portion of the survivor events. The disagreement demonstrated in Figure 4.10, however, is not negligible and could be indicative of the leakage events not being within the population of the survivor events. Complicating this comparison further is the disagreement between MC and data with a thorium source located outside of the steel shell (see Figure 4.11). This

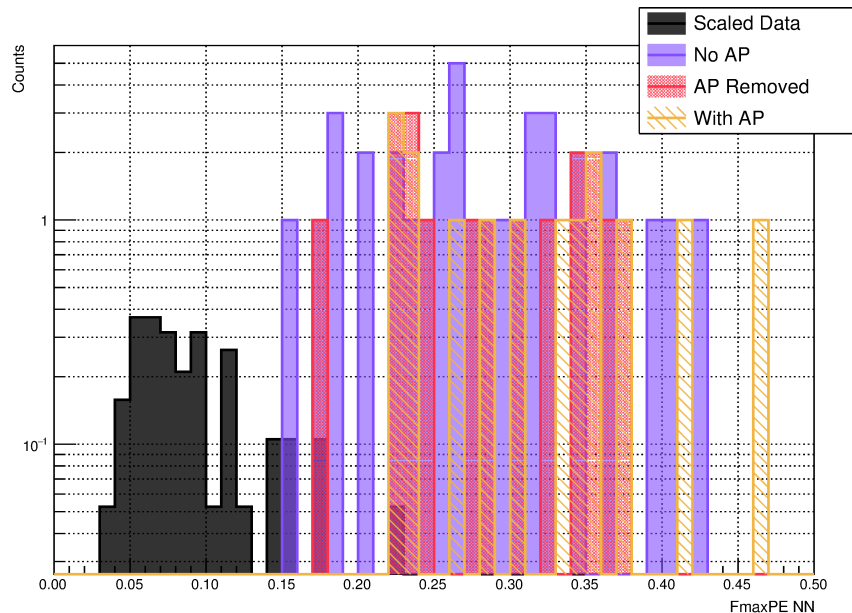


Figure 4.10: The distribution of $f_{\max pe}$ nearest neighbors for the leakage events of all three simulation sets as well as for the survivor events (scaled down by a factor of 19 to better match the livetime of the leakage events). Kolmogorov tests between leakage events and survivor events reinforce visual disagreement with values of 0.04, 0.04, and 0.03 for NAP, APR, and WAP events versus survivor events, respectively.

calibration source produces Cherenkov light in the acrylic from gamma interactions. It can be seen in Figure 4.11a that the tail of the Cherenkov light is much higher for data than MC. Figure 4.11b shows that the distribution of Cherenkov light in the detector also differs, with data detecting a much higher fraction of the light in a single PMT. These discrepancies pose a challenge for this research because the mechanism for the leakage events is highly dependent on how the light is distributed in the detector. The cause of the deviation between MC and data can be attributed primarily to two factors. Simulations of DEAP-3600 do not include acrylic fluorescence, which has been found to occur in the detector. There are also problems with the current optical model implemented in the simulation. Work is ongoing within the collaboration to improve the simulated behavior [56].

Even with the lower simulated light yield, there are still leakage events that survive the MC applicable cuts listed in Table 4.2, as well as the multisite cut. Calculating the number of leakage events for 95.79 days of livetime shows the population of the leakage events that could be in the survivor event set. This cut flow is shown in Table 4.3. The two major takeaways from this table are: two out of the three simulation sets have leakage events passing all of the cuts—meaning they would make up part of the survivor event population—and that the leakage events have a dependence on afterpulsing.

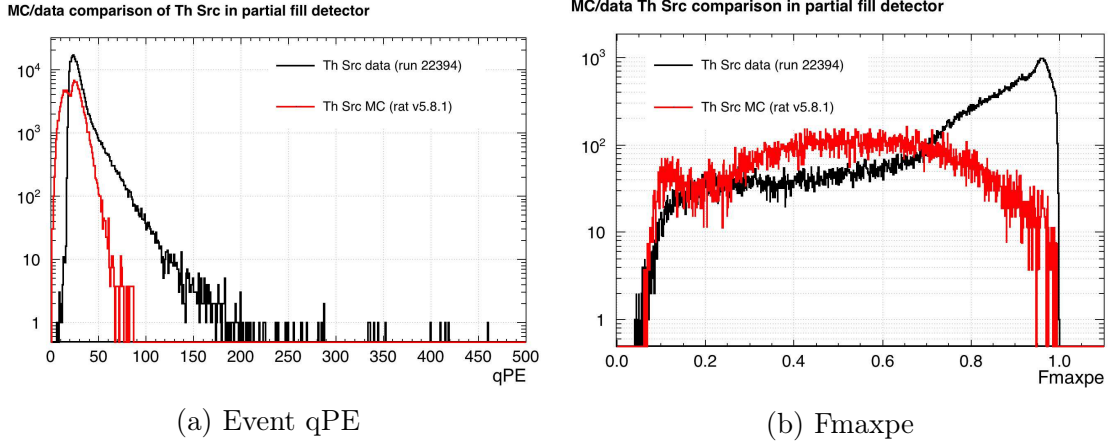


Figure 4.11: Comparison of data and simulation with a thorium source placed near the detector. The MC is normalized to the runtime of the data, which is 56 minutes. A cut to exclude events with event qPE < 25 PE was applied to the MC and data for the fmaxpe distribution. The small bump on the left side of the MC distributions is likely due to differences in the trigger settings between MC and data. Plots were created by Courtney Mielnichuk [57].

Table 4.3: The number of events for each simulation that survive the listed cuts, scaled to 95.79 days to match the livetime of the survivor events data set. The MBfitter radius cut is survived by: the events with a radius below 800 mm, 0.8% of events with a radius above 800 mm and with a charge ≤ 100 PE, and 0.5% of events with a radius above 800 mm with a charge > 100 PE. These percentages represent the rates that a data based study of MBfitter shows are misreconstructed at a radius ≥ 800 mm [58]. These rates are significantly smaller in MC, and thus are factored in to more closely emulate reality.

Cuts Applied	# of Events Remaining for:		
	No AP	AP Removed	With AP
MBfitter radius	105^{+70}_{-33}	29^{+52}_{-15}	15^{+37}_{-8}
Multisite, MBfitter radius	101^{+47}_{-49}	26^{+26}_{-19}	11^{+41}_{-4}
Fmaxpe ≤ 0.2 , Multisite, MBfitter radius	99^{+49}_{-47}	21^{+31}_{-14}	2^{+22}_{-2}
Top2ringsfrac ≤ 0.05 , Fmaxpe ≤ 0.2 , Multisite, MBfitter radius	79^{+49}_{-35}	21^{+31}_{-14}	2^{+22}_{-2}
Fmaxnsc ≤ 0.07 , Top2ringsfrac ≤ 0.05 , Fmaxpe ≤ 0.2 , Multisite, MBfitter radius	38^{+43}_{-24}	19^{+33}_{-12}	0^{+24}_{-0}

4.5 Effect of Afterpulsing on Leakage Events

It is quantitatively and qualitatively shown via Table 4.3 and Figure 4.8 that, once cuts are applied to the leakage events, there are more NAP and APR events left in the ROI than WAP events. This is an interesting, but concerning, observation as it implies that inaccuracy within the measurement improves the ability to cut events from the ROI. There are a few possible causes for this, relating to the accuracy of the simulations and the events themselves.

Table 4.4: The percentage of events removed by each individual cut out of all of the leakage events for each simulation type. Each reported efficiency represents the performance of the specific cut on the leakage events.

Cut	% of Events Cut for:		
	No AP	AP Removed	With AP
MBfitter Radius	94±14	98±16	99±14
Fmaxnsc	95±15	99±16	100±14
Fmaxpe	44±9	64±12	80±12
Top2ringsfrac	10±4	12±4	13±4
Multisite	39±8	30±7	29±6

As discussed in Section 4.4, the simulation of the energy in the detector is currently too low. This affects the overall amount of energy seen, as well as the distribution of that energy. All of the cuts listed in Table 4.4 relate in some way to the charge, and many are also directly related to the distribution of light. Both fmaxpe and fmaxnsc are related to the fraction of light in the highest charge PMT over the total light seen for the event. Top2ringsfrac is a measure of the amount of light in the gaseous area of the detector. It is therefore possible that these cuts, which are based on the data, are poorly calculated for the simulation.

Another simulation related factor could arise from incorrectly simulating the AP. The behavior in Figure 4.12 shows the expected increase in energy and decrease in F_{prompt} as the amount of AP increases (discussed in Section 3.2). This shift down and to the right is less prevalent when examining events at low energy. In Figure 4.13, the events appear to have a noticeably lower F_{prompt} without having a noticeable increase in energy.

It is possible that the addition of afterpulsing causes a secondary class of events to move into the ROI that are more easily removed by cuts. Table 4.1 shows that there are many more pure Cherenkov events within the ROI for the WAP dataset than for the APR and NAP datasets. As the fmaxpe cut is used to remove pure Cherenkov events, this means that the WAP simulation has a higher population of events for the cut to remove. When applying the cuts solely to the events with mixed Cherenkov and scintillation, some of the cut efficiencies become more similar for all of the simulations, such as fmaxpe and multisite.

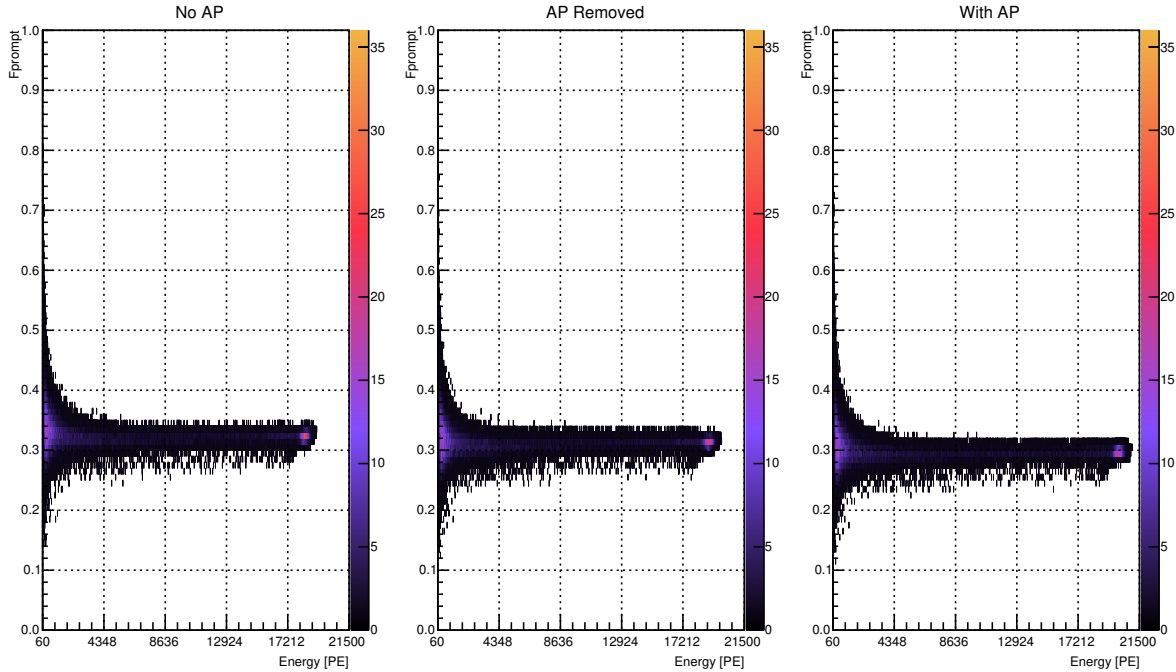


Figure 4.12: Plots of F_{prompt} vs energy for the four million PMT gammas. The plots have single PE binning and the energy range is from 60-21500 PE. Events below 60 PE are not included in order to see features within the plots. The color scale denotes the number of events in each bin.

It can be seen in Table 4.5 that the f_{maxpe} cut remains less efficient for NAP events, but the difference in efficiency between the simulations is less dramatic and some discrepancy is expected. This is both because the f_{maxpe} cut is also designed to remove high F_{prompt} AP and because the AP probability scales with the amount of incident light. The highest charge PMT will have the highest rate of afterpulsing, which will increase the event's f_{maxpe} .

The only cuts where the efficiencies became more different between all three simulations are fiducial-based: f_{maxnsc} and MBfitter radius. This observation requires further investigation since AP should not effect the position of the leakage events. This could be due in part to all of the current official position fitters depending on charge, indicating that a prompt timing-based position fitter might perform better. However, f_{maxnsc} is based solely on the amount of scintillation light and therefore should not be influenced by AP, though it does not have a correct hypothesis for the treatment of events that are a combination of Cherenkov and scintillation. That would again point to a problem in the simulation of the AP, but further analysis of how well the AP is simulated is outside the scope of this thesis.

This chapter has explained the mechanism of the leakage events, looked into the possibility of those events being in the ROI in data and laid out several possibilities for further study.

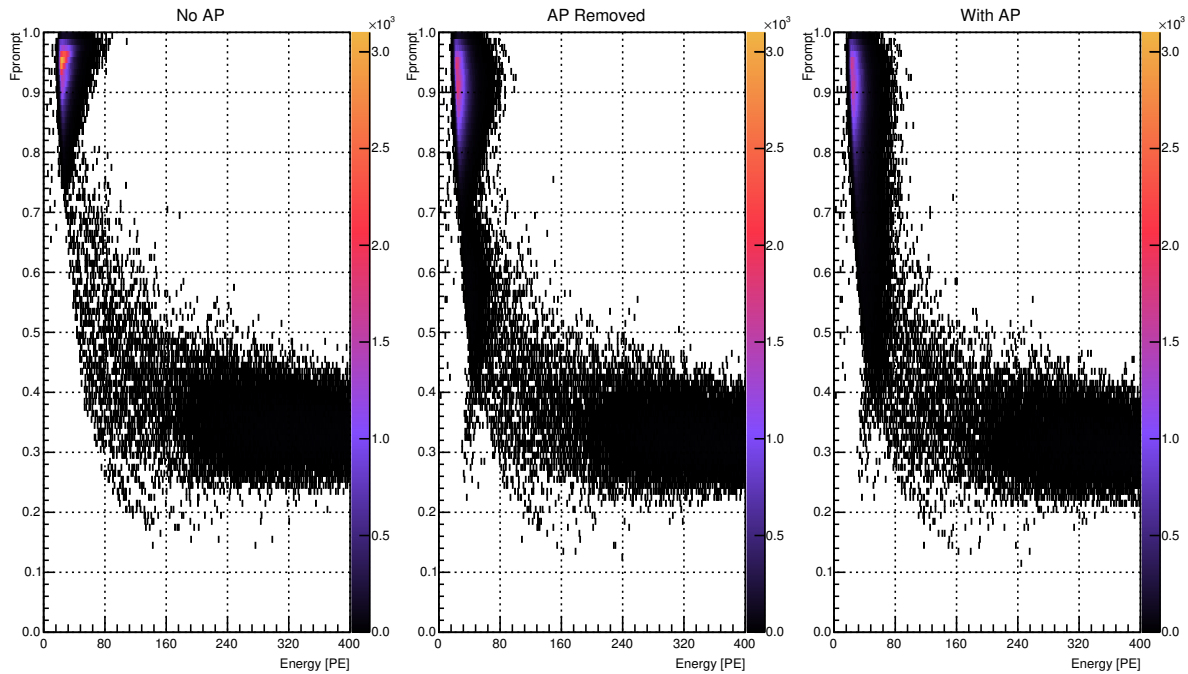


Figure 4.13: Plots of F_{prompt} vs energy that show the behavior of low energy events as the amount of AP decreases. All have single PE binning. The color scale denotes the number of events in each bin.

Table 4.5: The percentage of events removed by individual cuts from the leakage events that contain scintillation light. Each efficiency represents the performance of the individual cut on the leakage events.

Cut	% of Events Cut for:		
	No AP	AP Removed	With AP
MBfitter Radius	93±16	97±20	99±23
Fmaxnsc	95±16	98±20	100±24
Fmaxpe	36±8	45±12	44±13
Top2rings Frac	11±4	11±5	17±7
Multisite	41±9	43±11	42±13

Chapter 5

Conclusion

Dark matter remains to be detected beyond the observations of its gravitational effects. Due to its weakly interacting nature, direct detection experiments searching for evidence of WIMP dark matter require very low inherent background levels, including the ability to discriminate against persistent background events. This thesis has presented a study of the DEAP-3600 detector energy resolution and contributions of background events. Changes to the resolution were investigated with the gamma lines in the data when PMT corrections were applied. All of the improvements were found to be within uncertainty of the energy resolution of the raw charge, thus PMT corrections were found to have a negligible effect on the resolution of the gamma lines in the data. The resulting best energy resolution was that of the ^{208}Tl gamma line at $3.85 \pm 0.09\%$. In comparison, simulations showed that removing PMT afterpulsing lowered the energy resolution by $0.27 \pm 0.03\%$ to the resultant energy resolution of $2.59 \pm 0.02\%$. This provides evidence that an unaccounted factor (or factors) is dominating the energy resolution in data and causing variations in the relative channel gain and efficiency to be insignificant in comparison. Next steps for this research are to look at data taken with a gamma source near the detector to better compare the measured behavior with that of the simulations, as well as to explore the improvement of the energy resolution when using one of DEAP-3600's AP removal techniques. These avenues were not followed up during this research due to a lack of good quality gamma source data at the time. Further study into possible contributing factors to the energy resolution, such as taking into consideration the existence of a property of LAr adding a spatial component, is also needed.

The larger focus of this thesis centered on investigating the ability of high-energy gamma rays to mimic WIMP signals. It was determined that the most likely mechanism for high-energy gammas to leak into the WIMP ROI was from high-energy Compton scattering in the acrylic followed by a deposition of the remaining energy in the LAr. It was shown that

this led to more distribution of the light throughout the detector from an event, which cause cuts designed to remove background radiation to fail. A comparison was made to events that survive cuts in data, but the potential overlap of variables between simulation and data populations were inconclusive. It was shown, however, that the simulation does not correctly model the behavior of Cherenkov light in the detector, preventing a decisive conclusion from being made on whether or not events from data that remain in the ROI after cuts include a population of high-energy gamma rays.

This demonstrates the necessity of improving the DEAP-3600 simulations to better emulate the detector's behavior. Work is currently underway to improve the simulations, with an upgrade to the optics model having recently emerged after this research was concluded. Studies into how the new optics affects both the leakage of high-energy gammas into the WIMP ROI, and their similarity to data events, has already been proposed. Furthermore, while the largest source of 2.6 MeV gamma rays stem from the PMT glass, there are other sources to investigate including the steel neck vacuum jacket that extends almost to the LAr. This steel has significantly lower activity of ^{232}Th —the parent of the 2.6 MeV ^{208}Tl gamma emitter—but is also located much closer to the LAr than the PMTs, meaning it also has the opportunity to contribute to the leakage of high-energy gamma rays.

The effect of afterpulsing on the leakage event probability was also explored. It was determined that events without AP were more likely to be in the ROI. The fact that keeping afterpulsing in the events improves the ability to cut events in the ROI necessitates further study, as inaccuracy in the measurement should not increase the discrimination power of the detector. In future work, the way in which the AP is simulated will be altered so that afterpulses are tagged as their own population. At present, they are tagged as late pulses which prevents them from being removed from an existing simulation without also removing other types of late light. With a dedicated AP pulse type, a direct comparison of the same physics event could be made with and without afterpulsing. This would allow for a more comprehensive study of what elements in the addition of afterpulsing makes cuts on some variables more efficient, especially with respect to how it changes where the event is reconstructed in the detector.

References

- [1] V. Trimble, “Existence and nature of dark matter in the universe,” *Annual Review of Astronomy and Astrophysics*, vol. 25, no. 1, pp. 425–472, 1987. DOI: [10.1146/annurev.aa.25.090187.002233](https://doi.org/10.1146/annurev.aa.25.090187.002233). eprint: <https://doi.org/10.1146/annurev.aa.25.090187.002233>. [Cited On: 1]
- [2] J. B. Holberg, “Le verrier and the discovery of sirius b,” *Sky and Telescope*, Feb. 2008. [Cited On: 1]
- [3] R. S. Ellis, “Gravitational lensing: A unique probe of dark matter and dark energy,” *Philosophical Transactions of the Royal Society of London A: Mathematical, Physical and Engineering Sciences*, vol. 368, no. 1914, pp. 967–987, 2010, ISSN: 1364-503X. DOI: [10.1098/rsta.2009.0209](https://doi.org/10.1098/rsta.2009.0209). eprint: <http://rsta.royalsocietypublishing.org/content/368/1914/967.full.pdf>. [Cited On: 1]
- [4] F. Zwicky, “Die rotverschiebung von extragalaktischen nebeln,” trans. by H. Andernach, *Helvetica Physica Acta*, vol. 6, pp. 110–127, 1933. [Online]. Available: <http://ned.ipac.caltech.edu/level5/March17/Zwicky/frames.html>. [Cited On: 1]
- [5] D. H. DeVorkin and R. W. Smith, *The Hubble Cosmos: 25 Years of New Vistas in Space*. 1145 17th Street NW, Washington, DC 20036-4688 USA: National Geographic, Oct. 2015. [Cited On: 1]
- [6] G. Bertone and D. Hooper, “A History of Dark Matter,” *Submitted to: Rev. Mod. Phys.*, May 2016. arXiv: [1605.04909](https://arxiv.org/abs/1605.04909) [[astro-ph.CO](https://arxiv.org/abs/1605.04909)]. [Cited On: 1]
- [7] J. L. Feng, “Dark matter candidates from particle physics and methods of detection,” *Annual Review of Astronomy and Astrophysics*, vol. 48, no. 1, pp. 495–545, 2010. DOI: [10.1146/annurev-astro-082708-101659](https://doi.org/10.1146/annurev-astro-082708-101659). eprint: <https://doi.org/10.1146/annurev-astro-082708-101659>. [Cited On: 2, 3]
- [8] S. van den Bergh, “Cosmology - In search of a new paradigm,” *Journal of the Royal Astronomical Society of Canada*, vol. 84, pp. 275–280, 1990. [Cited On: 2]
- [9] P. A. R. Ade, N. Aghanim, M. Arnaud, *et al.*, “Planck2015 results,” *Astronomy & Astrophysics*, vol. 594, A13, Sep. 2016, ISSN: 1432-0746. DOI: [10.1051/0004-6361/201525830](https://doi.org/10.1051/0004-6361/201525830). [Online]. Available: <http://dx.doi.org/10.1051/0004-6361/201525830>. [Cited On: 2]

- [10] P.-A. Amaudruz, M. Baldwin, M. Batygov, *et al.*, “First results from the deap-3600 dark matter search with argon at snolab,” *Phys. Rev. Lett.*, vol. 121, p. 071801, 7 Aug. 2018. DOI: [10.1103/PhysRevLett.121.071801](https://doi.org/10.1103/PhysRevLett.121.071801). [Online]. Available: <https://link.aps.org/doi/10.1103/PhysRevLett.121.071801>. [Cited On: 2, 4, 15, 19, 21, 29]
- [11] D. G. Cerdeno and A. M. Green, “Direct detection of wimps,” in *Particle Dark Matter: Observations, Models and Searches*, G. Bertone, Ed. The Edinburgh Building, Cambridge CB2 8RU, UK: Cambridge University Press, 2010, ch. 17, pp. 121–141. [Cited On: 2]
- [12] V. A. Mitsou, “Overview of searches for dark matter at the lhc,” *Journal of Physics: Conference Series*, vol. 651, no. 1, p. 012023, 2015. [Online]. Available: <http://stacks.iop.org/1742-6596/651/i=1/a=012023>. [Cited On: 2]
- [13] M. G. Aartsen *et al.*, “Search for Neutrinos from Dark Matter Self-Annihilations in the center of the Milky Way with 3 years of IceCube/DeepCore,” *Eur. Phys. J.*, vol. C77, no. 9, p. 627, 2017. DOI: [10.1140/epjc/s10052-017-5213-y](https://doi.org/10.1140/epjc/s10052-017-5213-y). arXiv: [1705.08103](https://arxiv.org/abs/1705.08103) [hep-ex]. [Cited On: 2]
- [14] K. Frankiewicz and S.-K. collaboration, “Dark matter searches with the super-kamiokande detector,” *Journal of Physics: Conference Series*, vol. 888, no. 1, p. 012210, 2017. [Cited On: 3]
- [15] L. Roszkowski, E. M. Sessolo, and S. Trojanowski, “Wimp dark matter candidates and searches—current status and future prospects,” *Reports on Progress in Physics*, vol. 81, no. 6, p. 066201, 2018. [Online]. Available: <http://stacks.iop.org/0034-4885/81/i=6/a=066201>. [Cited On: 3]
- [16] R. W. Schnee, “Introduction to dark matter experiments,” in *Physics of the Large and the Small*. World Scientific, 2012, pp. 775–829. DOI: [10.1142/9789814327183_0014](https://doi.org/10.1142/9789814327183_0014). eprint: https://www.worldscientific.com/doi/pdf/10.1142/9789814327183_0014. [Cited On: 3–5, 7, 9]
- [17] J. Formaggio and C. Martoff, “Backgrounds to sensitive experiments underground,” *Annual Review of Nuclear and Particle Science*, vol. 54, pp. 361–412, Nov. 2004. [Cited On: 3, 15–18]
- [18] T. M. Undagoitia and L. Rauch, “Dark matter direct-detection experiments,” *Journal of Physics G: Nuclear and Particle Physics*, vol. 43, no. 1, p. 013001, 2016. [Online]. Available: <http://stacks.iop.org/0954-3899/43/i=1/a=013001>. [Cited On: 4, 5, 9]
- [19] C. Amole, M. Ardid, I. J. Arnquist, *et al.*, “Dark Matter Search Results from the PICO-60 C₃F₈ Bubble Chamber,” *Phys. Rev. Lett.*, vol. 118, p. 251301, 25 Jun. 2017. DOI: [10.1103/PhysRevLett.118.251301](https://doi.org/10.1103/PhysRevLett.118.251301). [Online]. Available: <https://link.aps.org/doi/10.1103/PhysRevLett.118.251301>. [Cited On: 4]
- [20] L. Baudis, *Lecture 3: Direct detection techniques and experiments, i*, Online Lecture, Mar. 2012. [Online]. Available: http://fma.if.usp.br/~burdman/DM/Laura_3.pdf. [Cited On: 4, 5]

- [21] L. Baudis, *Lecture 4: Direct detection techniques and experiments, ii*, Online Lecture, Mar. 2012. [Online]. Available: http://fma.if.usp.br/~burdman/DM/Laura_4.pdf. [Cited On: 5, 9]
- [22] D. Gastler, E. Kearns, A. Hime, *et al.*, “Measurement of scintillation efficiency for nuclear recoils in liquid argon,” *Phys. Rev. C*, vol. 85, p. 065 811, 6 Jun. 2012. DOI: [10.1103/PhysRevC.85.065811](https://doi.org/10.1103/PhysRevC.85.065811). [Online]. Available: <https://link.aps.org/doi/10.1103/PhysRevC.85.065811>. [Cited On: 6, 7]
- [23] A. Hallin, Private Communication, Sep. 2018. [Cited On: 6]
- [24] E. Aprile and L. Baudis, “Liquid noble gases,” in *Particle Dark Matter: Observations, Models and Searches*, G. Bertone, Ed. The Edinburgh Building, Cambridge CB2 8RU, UK: Cambridge University Press, 2010, ch. 21, pp. 413–436. [Cited On: 6, 9]
- [25] V. Chepel and H. Araújo, “Liquid noble gas detectors for low energy particle physics,” *Journal of Instrumentation*, vol. 8, no. 04, R04001, Apr. 2013. [Online]. Available: <http://stacks.iop.org/1748-0221/8/i=04/a=R04001>. [Cited On: 7]
- [26] S. S. Westerdale, “A study of nuclear recoil backgrounds in dark matter detectors,” PhD thesis, Princeton University, Nov. 2016. [Cited On: 7]
- [27] V. Gehman, S. Seibert, K. Rielage, *et al.*, “Fluorescence efficiency and visible re-emission spectrum of tetraphenyl butadiene films at extreme ultraviolet wavelengths,” *Nuclear Instruments and Methods in Physics Research Section A: Accelerators, Spectrometers, Detectors and Associated Equipment*, vol. 654, no. 1, pp. 116–121, Oct. 2011, ISSN: 0168-9002. DOI: <https://doi.org/10.1016/j.nima.2011.06.088>. [Online]. Available: <http://www.sciencedirect.com/science/article/pii/S0168900211013271>. [Cited On: 7, 11]
- [28] A. Hitachi, T. Takahashi, N. Funayama, *et al.*, “Effect of ionization density on the time dependence of luminescence from liquid argon and xenon,” *Phys. Rev. B*, vol. 27, pp. 5279–5285, 9 May 1983. DOI: [10.1103/PhysRevB.27.5279](https://doi.org/10.1103/PhysRevB.27.5279). [Online]. Available: <https://link.aps.org/doi/10.1103/PhysRevB.27.5279>. [Cited On: 7]
- [29] P.-A. Amaudruz, M. Batygov, B. Beltran, *et al.*, “Measurement of the scintillation time spectra and pulse-shape discrimination of low-energy β and nuclear recoils in liquid argon with deap-1,” *Astroparticle Physics*, vol. 85, pp. 1–23, 2016, ISSN: 0927-6505. DOI: <https://doi.org/10.1016/j.astropartphys.2016.09.002>. [Online]. Available: <http://www.sciencedirect.com/science/article/pii/S0927650516301232>. [Cited On: 8, 11]
- [30] B. Lehnert, “Backgrounds in the deap-3600 dark matter experiment,” in *15th International Conference on Topics in Astroparticle and Underground Physics (TAUP 2017) Sudbury, Ontario, Canada, July 24-28, 2017*, May 2018. eprint: [1805.06073](https://arxiv.org/abs/1805.06073). [Online]. Available: <https://arxiv.org/pdf/1805.06073>. [Cited On: 8, 15–19]
- [31] P.-A. Amaudruz, M. Baldwin, M. Batygov, *et al.*, “Design and Construction of the DEAP-3600 Dark Matter Detector,” *Submitted to: Astropart. Phys.*, 2017. arXiv: [1712.01982](https://arxiv.org/abs/1712.01982) [astro-ph.IM]. [Cited On: 9–16, 18, 21, 22]

- [32] *Photomultiplier tubes: Basics and applications*, 3a, Hamamatsu Photonics K. K., 2007. [Cited On: 11, 28]
- [33] “Large photocathode area photomultiplier tubes,” Hamamatsu Photonics, 314-5, Shimokanzo, Iwata City, Shizuoka Pref., 438-0193, Japan, Datasheet, Jan. 2016. [Online]. Available: https://www.hamamatsu.com/resources/pdf/etd/LARGE_AREA_PMT_TPMH1286E.pdf. [Cited On: 11]
- [34] P. Amaudruz, M. Batygov, B. Beltrán, *et al.*, “In-situ characterization of the Hamamatsu R5912-HQE photomultiplier tubes used in the DEAP-3600 experiment,” 2017. arXiv: [1705.10183](https://arxiv.org/abs/1705.10183) [physics.ins-det]. [Cited On: 11, 12, 23, 24]
- [35] G. F. Knoll, *Radiation detection and measurement*, 4th. Hoboken, N.J.: John Wiley, 2010. [Cited On: 12, 18, 20]
- [36] B. R. Martin, *Nuclear and Particle Physics*, 2nd. John Wiley & Sons Ltd, The Atrium, Southern Gate, Chichester, West Sussex, PO19 8SQ, UK: Wiley, Mar. 2009. [Cited On: 12]
- [37] B. Smith, *Daq overview*, Presentation given at DEAP DAQ Training, May 2017. [Cited On: 13]
- [38] T. Pollmann, “Alpha backgrounds in the deap dark matter search experiment,” PhD thesis, Queen’s University, Aug. 2012. [Cited On: 16–18]
- [39] B. Cai, M. Boulay, M. Kuzniak, *et al.*, “Neutron backgrounds in deap-3600,” DEAP Collaboration, Internal Document, DEAP3600-STR-2011-009-Rev2, Dec. 2011. [Cited On: 18]
- [40] P. Benetti, F. Calaprice, E. Calligarich, *et al.*, “Measurement of the specific activity of ^{39}Ar in natural argon,” *Nuclear Instruments and Methods in Physics Research Section A: Accelerators, Spectrometers, Detectors and Associated Equipment*, vol. 574, no. 1, pp. 83–88, 2007, ISSN: 0168-9002. DOI: <https://doi.org/10.1016/j.nima.2007.01.106>. [Online]. Available: <http://www.sciencedirect.com/science/article/pii/S0168900207001672>. [Cited On: 19]
- [41] A. Lubashevskiy, M. Agostini, D. Budjas, *et al.*, “Mitigation of $^{42}\text{Ar}/^{42}\text{K}$ background for the gerda phase ii experiment,” *The European Physical Journal C*, vol. 78, Aug. 2017. [Cited On: 19]
- [42] *Radiation detectors*, Online Lecture, 2011. [Online]. Available: <http://radchem.nevada.edu/classes/rfss/lectures/Lect%2011%20-%20Radiation%20Detectors.pdf>. [Cited On: 20]
- [43] N. Fatemighomi, S. Langrock, R. Mehdiyev, *et al.*, “Energy response of deap-3600,” DEAP Collaboration, Internal Document, DEAP3600-STR-2017-06, 2017. [Cited On: 21, 24]
- [44] R. Stainforth, “Cuts and acceptances,” DEAP Collaboration, Internal Document, DEAP3600-STR-2017-013-Rev-A2, Oct. 2017. [Cited On: 21, 44]
- [45] T. McElroy, *Peak finding*, Presentation given at DEAP Analysis Workshop, Oct. 2016. [Cited On: 21]

- [46] B. Lehnert, “Light yield fits during lar filling,” DEAP Collaboration, Internal Document 132-v3, 2016. [Cited On: 24]
- [47] S. Seibert, T. Bolton, D. Gastler, *et al.*, *Rat documentation, release 1.0*, Feb. 2018. [Online]. Available: <https://rat.readthedocs.io/en/latest/overview.html>. [Cited On: 29, 34]
- [48] G. Horton-Smith, *Introduction to glg4sim*, Online Presentation, May 2006. [Online]. Available: <http://puhep1.princeton.edu/~mcdonald/dayabay/Horton-Smith/GLG4sim-intro-2006-05-19.pdf>. [Cited On: 29]
- [49] T. Caldwell, *Simulation of noble liquid detectors using rat*, Online Presentation, Mar. 2014. [Online]. Available: https://zzz.physics.umn.edu/lowrad/_media/meeting7/rat_aarm_2014.pdf. [Cited On: 29]
- [50] *Live chart of nuclides*. [Online]. Available: <https://www-nds.iaea.org/relnsd/vcharthtml/VChartHTML.html>. [Cited On: 29]
- [51] “Full details of specific background normalisations,” DEAP Collaboration, Internal Document, Sep. 2016. [Online]. Available: <https://www.snolab.ca/deap/private/TWiki/pub/Main/MasterBackgrounds/Normalisation.pdf>. [Cited On: 29]
- [52] “Master cuts page,” DEAP Collaboration, Internal Document, 2018. [Online]. Available: <https://www.snolab.ca/deap/private/TWiki/bin/view/Main/MasterCutsPage>. [Cited On: 37, 44]
- [53] T. McElroy, “Multisite usage,” DEAP Collaboration, Internal Document 241-v1, Aug. 2017. [Cited On: 40, 41]
- [54] R. Stainforth, “Good run list,” Carleton University, Internal Document, 2017. [Online]. Available: https://www.snolab.ca/deap/private/TWiki/pub/DEAP3/AnalysisNotex220/GoodRunList_fromRob.txt. [Cited On: 43]
- [55] J. Bueno, “Uofa cut flow,” DEAP Collaboration, Internal Document 215-v3, Apr. 2017. [Cited On: 44]
- [56] P. Giampa, D. Geoldi, P. Gorel, *et al.*, “Optical model of deap-3600 and monte carlo simulation validation,” DEAP Collaboration, Internal Document, DEAP3600-STR-2018-005, Aug. 2018. [Cited On: 46]
- [57] C. Mielnichuk, Private Communication, Jun. 2018. [Cited On: 47]
- [58] J. Willis, *Testing the mblikelihood fitter*, Presentation given at the DEAP Collaboration meeting, Sudbury, ON, Sep. 2017. [Cited On: 47]

Appendix A

Sample Track

This is an example of a track for a single simulated gamma stemming from a PMT. The structure for each line is: current step/total number of steps: process taken in that step, name of the detector volume the process occurs in, the kinetic energy of the particle after undergoing the process, the coordinates of the particle in mm.

```

0/73: start, PMTs178, KE=2.61453, (x,y,z)=-950.304,940.156,-598.272
1/73: Transportation, PMTs178, KE=2.61453, (x,y,z)=-949.472,939.648,-597.789
2/73: Transportation, PMTs_inner2_phys, KE=2.61453,
      (x,y,z)=-922.129,922.961,-581.935
3/73: Transportation, PMTs_central_gap_phys, KE=2.61453,
      (x,y,z)=-922.129,922.961,-581.935
4/73: Transportation, PMTs_inner1_phys, KE=2.61453,
      (x,y,z)=-878.041,896.054,-556.372
5/73: Transportation, PMTs178, KE=2.61453, (x,y,z)=-874.852,894.108,-554.523
6/73: compt, LGs_178, KE=2.46231, (x,y,z)=-624.605,741.383,-409.426
7/73: compt, LGs_178, KE=0.500518, (x,y,z)=-556.029,681.276,-360.845
8/73: Transportation, LGs_178, KE=0.500518, (x,y,z)=-514.484,645.036,-429.413
9/73: Transportation, vac_filler, KE=0.500518, (x,y,z)=-514.464,645.02,-429.445
10/73: Transportation, LG_refls_178_0, KE=0.500518,
      (x,y,z)=-514.429,644.988,-429.504
11/73: Transportation, vac_filler, KE=0.500518, (x,y,z)=-511.75,642.652,-433.925
12/73: Transportation, filler_insulation1, KE=0.500518,
      (x,y,z)=-505.725,637.396,-443.869
13/73: compt, filler, KE=0.40229, (x,y,z)=-469.753,606.019,-503.237
14/73: Transportation, filler, KE=0.40229, (x,y,z)=-464.595,605.737,-505.333
15/73: Transportation, vac_filler, KE=0.40229, (x,y,z)=-464.04,605.707,-505.559

```

16/73: Transportation, filler, KE=0.40229, (x,y,z)=-447.818,604.822,-512.151
17/73: Transportation, vac_filler, KE=0.40229, (x,y,z)=-431.93,603.955,-518.607
18/73: Transportation, LG_refls_193_0, KE=0.40229,
(x,y,z)=-431.638,603.939,-518.725
19/73: Transportation, vac_filler, KE=0.40229, (x,y,z)=-431.479,603.93,-518.79
20/73: Transportation, LGs_193, KE=0.40229, (x,y,z)=-416.287,603.101,-524.963
21/73: compt, av, KE=0.329068, (x,y,z)=-213.116,592.014,-607.52
22/73: compt, av, KE=0.205185, (x,y,z)=-203.566,586.709,-628.592
23/73: compt, av, KE=0.181359, (x,y,z)=-203.489,586.705,-628.562
24/73: compt, av, KE=0.16072, (x,y,z)=-198.588,586.145,-630.997
25/73: compt, av, KE=0.149563, (x,y,z)=-193.254,590.892,-631.698
26/73: Transportation, av, KE=0.149563, (x,y,z)=-187.856,603.49,-642.746
27/73: Transportation, vac_filler, KE=0.149563, (x,y,z)=-187.853,603.498,-642.753
28/73: Transportation, outercoat, KE=0.149563, (x,y,z)=-187.817,603.581,-642.826
29/73: Transportation, vac_filler, KE=0.149563, (x,y,z)=-185.602,608.752,-647.36
30/73: Transportation, filler, KE=0.149563, (x,y,z)=-178.869,624.463,-661.137
31/73: Transportation, filler_insulation1, KE=0.149563,
(x,y,z)=-174.406,634.88,-670.272
32/73: compt, filler, KE=0.0985103, (x,y,z)=-172.836,638.543,-673.484
33/73: Transportation, filler, KE=0.0985103, (x,y,z)=-175.042,631.255,-673.522
34/73: Transportation, filler_insulation1, KE=0.0985103,
(x,y,z)=-180.656,612.708,-673.619
35/73: Transportation, vac_filler, KE=0.0985103, (x,y,z)=-182.579,606.355,-673.652
36/73: Transportation, LG_refls_229_1, KE=0.0985103,
(x,y,z)=-182.605,606.27,-673.652
37/73: Transportation, vac_filler, KE=0.0985103, (x,y,z)=-182.618,606.224,-673.652
38/73: Transportation, LGs_229, KE=0.0985103, (x,y,z)=-194.727,566.22,-673.861
39/73: compt, av, KE=0.0953644, (x,y,z)=-220.124,482.315,-674.297
40/73: compt, av, KE=0.087478, (x,y,z)=-218.891,475.139,-671.397
41/73: Transportation, av, KE=0.087478, (x,y,z)=-218.493,474.867,-671.538
42/73: Transportation, tpb_bulk, KE=0.087478, (x,y,z)=-218.484,474.862,-671.541
43/73: compt, cryoliquid, KE=0.0730592, (x,y,z)=-212.586,470.827,-673.63
44/73: Transportation, cryoliquid, KE=0.0730592, (x,y,z)=-212.445,472.459,-675.163
45/73: Transportation, tpb_bulk, KE=0.0730592, (x,y,z)=-212.445,472.461,-675.166
46/73: compt, av, KE=0.0677972, (x,y,z)=-210.241,498.105,-699.257
47/73: Transportation, av, KE=0.0677972, (x,y,z)=-232.079,508.469,-707.255
48/73: compt, LGs_229, KE=0.0658339, (x,y,z)=-261.195,522.288,-717.92
49/73: Transportation, LGs_229, KE=0.0658339, (x,y,z)=-266.784,520.964,-722.491

50/73: Transportation, vac_filler, KE=0.0658339, (x,y,z)=-266.823,520.955,-722.523
51/73: Transportation, LG_refls_229_1, KE=0.0658339,
(x,y,z)=-266.895,520.938,-722.581
52/73: Transportation, vac_filler, KE=0.0658339, (x,y,z)=-272.232,519.674,-726.946
53/73: Transportation, filler_insulation1, KE=0.0658339,
(x,y,z)=-278.991,518.073,-732.474
54/73: Transportation, filler, KE=0.0658339, (x,y,z)=-339.681,503.698,-782.112
55/73: Transportation, filler_insulation2, KE=0.0658339,
(x,y,z)=-354.187,500.262,-793.977
56/73: compt, filler, KE=0.0567946, (x,y,z)=-360.846,498.684,-799.423
57/73: Transportation, filler, KE=0.0567946, (x,y,z)=-357.959,493.358,-799.117
58/73: Transportation, vac_filler, KE=0.0567946, (x,y,z)=-354.994,487.889,-798.803
59/73: Transportation, LG_refls_238_0, KE=0.0567946,
(x,y,z)=-354.955,487.816,-798.799
60/73: Transportation, vac_filler, KE=0.0567946, (x,y,z)=-354.934,487.777,-798.797
61/73: compt, LGs_238, KE=0.0557632, (x,y,z)=-341.063,462.186,-797.328
62/73: compt, LGs_238, KE=0.0539911, (x,y,z)=-339.72,460.565,-798.489
63/73: compt, LGs_238, KE=0.0456057, (x,y,z)=-319.96,406.864,-785.583
64/73: compt, LGs_238, KE=0.0429632, (x,y,z)=-327.107,414.578,-781.058
65/73: compt, LGs_238, KE=0.041227, (x,y,z)=-332.172,427.45,-795.356
66/73: compt, LGs_238, KE=0.0362627, (x,y,z)=-295.112,464.154,-813.879
67/73: compt, LGs_238, KE=0.0323942, (x,y,z)=-311.221,455.581,-821.73
68/73: Transportation, LGs_238, KE=0.0323942, (x,y,z)=-302.901,472.417,-783.323
69/73: Transportation, vac_filler, KE=0.0323942, (x,y,z)=-302.89,472.437,-783.276
70/73: Transportation, LG_refls_238_0, KE=0.0323942,
(x,y,z)=-302.872,472.475,-783.189
71/73: Transportation, vac_filler, KE=0.0323942, (x,y,z)=-301.456,475.34,-776.655
72/73: compt, filler, KE=0.0322765, (x,y,z)=-298.556,481.209,-763.267
73/73: phot, filler, KE=0, (x,y,z)=-294.393,498.592,-744.903